Localized Antiaromaticity Hot-spot Drives Reductive Dehydrogenative Cyclizations in Bis- and Mono-Helicenes

Zheng Zhou,[a][b] Dominic T. Egger,[c] Chaowei Hu,[d] Matthew Pennachio,[a] Zheng Wei,[a] Rahul K. Kawade, [d] Ökten Üngör,[d] Renana Gershoni-Poranne,*[c][e] Marina A. Petrukhina,*[a] and Igor V. Alabugin*[d]

[a] Department of Chemistry, University at Albany, State University of New York, Albany, NY 12222, USA, e-mail: mpetrukhina@albany.edu

[b] School of Materials Science and Engineering, Tongji University, Shanghai 201804, China

[c] Laboratory for Organic Chemistry, Department of Chemistry and Applied Biosciences, ETH Zurich, Zurich 8903, Switzerland

[d] Department of Chemistry and Biochemistry, Florida State University, Tallahassee, FL 32306, USA, e-mail: alabugin@chem.fsu.edu

[e] Schulich Faculty of Chemistry, Technion — Israel Institute of Technology, Technion City 32000, Israel, e-mail: rporanne@technion.ac.il.

Abstract: We describe reductive dehydrogenative cyclizations that form hepta-, nona- and decacyclic anionic graphene subunits from mono- and bis-helicenes with an embedded five-membered ring. The reaction of bis-helicenes can either proceed to the full double annulation or be interrupted by addition of molecular oxygen at an intermediate stage. The regioselectivity of the interrupted cyclization cascade for bis-helicenes confirms that relief of antiaromaticity is a dominant force for these facile ring closures. Computational analysis reveals the unique role of the preexisting negatively charged cyclopentadienyl moiety in directing the 2nd negative charge at a specific remote location and, thus, creating a localized antiaromatic region. This region is the hot-spot that promotes the initial cyclization. Computational studies, including MO analysis, molecular electrostatic potential maps, and NICS(1.7)$_{ZZ}$ calculations evaluate the interplay of the various effects including charge delocalization, helicene strain release, and antiaromaticity. The role of antiaromaticity relief is further supported by efficient reductive closure of the less strained mono-helicenes where the relief of antiaromaticity promotes the cyclization even when the strain is substantially reduced. The latter finding significantly expands the scope of this reductive alternative to the Scholl ring closure.

Introduction

The archetypal description of graphene is the infinite sheet composed of hexagons. By cutting "substructures" from this infinite sheet, a vast number of carbon-rich polyaromatics of different shapes and sizes can be imagined (and synthesized via a suitable bottom-up approach).[1–13] However, in all this vast variety, it is the benzene ring that continues to serve as the dominant structural element. Rings of different size are introduced less frequently – usually with the goal of adding structural variations.[14–17] For example, the five- and seven-membered rings introduce a positive or a negative curvature, respectively. The five-membered rings (pentagons) are particularly common at highly curved locations in polyaromatics, such as in fullerenes or caps of closed carbon nanotubes.[18–34]

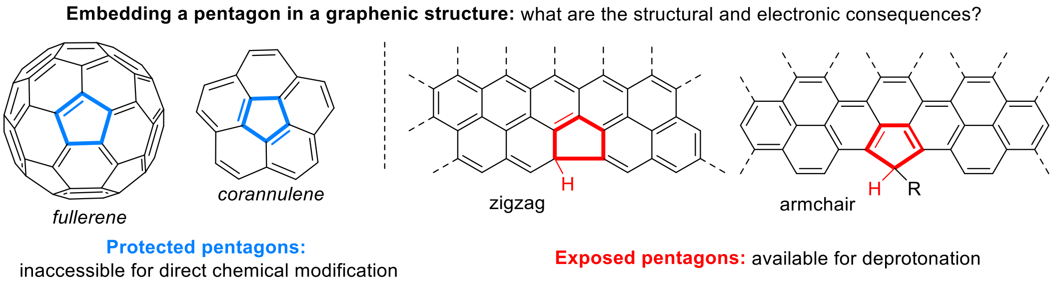

Figure 1. Two types of five-membered units in carbon-rich structures and the potential for insertion of pentagons in the classic graphenic sheet.

The pentagons that are fully embedded into a polycyclic network (i.e., C_{60} or corannulene) cannot undergo direct chemical modification without disrupting conjugation in their π-systems. Nevertheless, one can imagine that a five-membered ring at the edge of a graphenic structure may have an "exposed" sp^3 C-H site that is available for deprotonation. Such a feature can be useful for adding a negative charge to a conjugated system without simultaneously injecting a spin (Figure 1). The anionic center can be used for supramolecular assembly, metal coordination, etc.

In this context, we were intrigued to discover that it is possible to incorporate a pentagon at the edge of a decacyclic fused polyaromatic system by using reductive annulation of fused helicenes.[35] The key helicene precursors are readily assembled from oligoalkynes in a radical cascade that forms a five-membered ring.[36] Conveniently, this ring also contains a relatively acidic C-H bond. Deprotonation at this position can be followed by electron injection to the aromatic core, which forms an antiaromatic helicene radical-dianion. Unusually, such highly reducing conditions lead to a cascade of two dehydrogenative cyclizations, a formally oxidative process. The product of this cascade is a remarkable fully-fused dianion, which can be considered as a graphene substructure with an embedded cyclopentadienyl moiety. This decacyclic unit is flat despite the presence of a five-membered ring, i.e., the structural element that is associated with curvature in carbon-nanostructures.

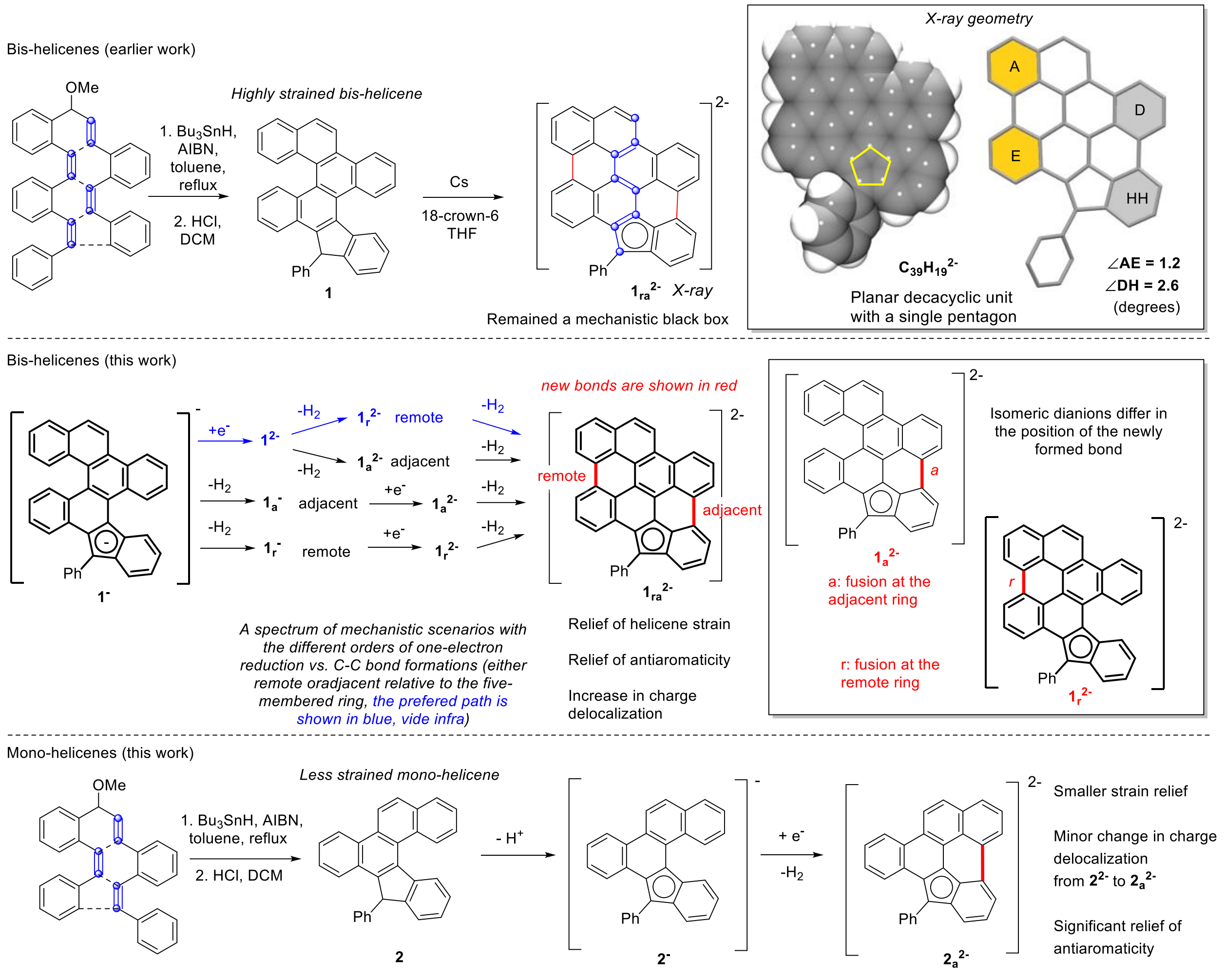

Scheme 1. Top: Deprotonation, reduction, and two-fold annulation of **1**; Middle: Possible mechanistic scenarios for two-fold annulation of bis-helicene **1** with the preferred path shown in blue. Bottom: Deprotonation, reduction, and annulation of mono-helicene **2.**

To make it even more intriguing, this species can be isolated and characterized, even though it bears two negative charges and an unpaired electron. Such unusual structural features offer interesting design opportunities for the development of hybrid organic/inorganic structures and materials. From a practical perspective, this reductive transformation provides a conceptually interesting alternative to the most common oxidative approach to fusing the aromatic rings together, the Scholl reaction. Despite the development of new reagents and continuous refinement and expansion of mechanistic scenarios,[37–41] this popular approach suffers from a number of drawbacks including a relatively narrow scope, occasionally unpredictable selectivity, and the existence of side reactions (chlorination, oxidation, rearrangements, and formation of oligomers via *inter*molecular couplings).[42] Additionally, activating groups are often needed to facilitate the redox chemistry.

The potential of conceptually new approaches to aromatic fusion is illustrated by emerging C-H activation strategies[43] and reactions at metallic surfaces.[44–47] However, many C-H activations are thermodynamically unfavorable. Strained helicene precursors can alleviate this problem. Indeed, our earlier computational analysis revealed that this remarkable transformation benefits from the favorable combination of helicene strain release, escape from antiaromaticity, and increased delocalization of the negative charge.[35]

In our preliminary report,[35] we described the isolation and full characterization of the initial deprotonated species (the monoanion $\mathbf{1}^{-}$) and the fully cyclized dianion $\mathbf{1_{ra}}^{2-}$ formed from a bis-helicene. These species correspond to the starting and finishing points of this reductive cascade. However, the rest of the reaction cascade remained a mechanistic black box. Although it is clear that this cascade involves two cyclizations and introduction of two negative charges, these observations left room for several mechanistic pathways (including sequences A-C outlined in Scheme 1) which differ in the charge state of the cyclizing species (monoanion or dianion) and in the regioselectivity of the first ring closure (close to or remote from the cyclopentadienyl anionic subunit). The fundamental importance of these mechanistic details lies in understanding the role of localized antiaromaticity in inducing these reductive cyclizations (*vide infra*).

The first insights into the black box were obtained from our initial computational analysis. It provided an intriguing prediction that the 1st cyclization in the bis-helicene system should proceed at a part that is remote from the pentagonal unit. In order to test this prediction experimentally, we sought a way to interrupt the bis-annulation cascade process at the first stage.

In particular, we wanted to: a) experimentally elucidate the sequence of the two cyclizations in the bis-helicene system and obtain additional experimental information regarding the charge state (anion or dianion) needed to promote the cyclization step and b) expand the scope of this new reductive dehydrogenative cyclization to significantly less strained *mono*-helicenes. From the conceptual perspective, we were interested in taking full advantage of computational analysis for exploring the relative roles of strain, antiaromaticity, and charge delocalization for gaining deeper insights into the mechanism for the reductive dehydrogenative coupling. Our broader goals are to develop approaches to introduce charge into graphenic materials (either with or without introducing spin) and to understand the interplay of geometric and electronic features in negatively charged open- and closed-shell polyaromatics.

Results and Discussion

Helicenes are helically shaped chiral polycyclic aromatic compounds.[48–55] Their inherent twist originates from their intramolecular steric demands and leads to special optical and electronic properties,[56–73] in comparison to their non-twisted counterparts. Deviations from planarity are generally associated with geometric distortions and with increased strain in these polycyclic structures. The properties of helicenes can be also affected by “defects”, such as variations in the ring size[36,74–79], the presence of heteroatoms,[80–89] and multi-electron addition.[17,90,91]

Strain is an intrinsic property of helicenes and presents an additional challenge in their synthesis. In order to overcome this challenge, one needs to start with high-energy precursors. In this context, alkynes provide a high-energy functionality that is also carbon-rich and, hence, is especially useful for the construction of diverse carbon-rich polycyclic aromatic frameworks.[92–101] Indeed, both the mono-helicene **2** and the fused bis[5]-helicene **1** were prepared from the respective tri-alkyne and tetra-alkyne precursors *via* the analogous Sn-mediated radical cascade (Scheme 1).[36]

Interrupted cyclization of bis-helicene. Although capturing a transient carbanionic intermediate before it undergoes a facile intramolecular reaction is intrinsically challenging, the interruption of this reduction/cyclization cascade was made possible by recognizing the importance of color changes along the reaction path. The first step of the Cs-induced reaction of **1** is deprotonation accompanied by the appearance of a deep red color. Upon further reduction, the reaction color changes from red to red-brown, and finally to dark brown. We found that the intermediate red-brown reaction solution is transformed into a green suspension upon treatment with a trace of O_2. By using slow diffusion of hexanes into the THF reaction solution in the presence of 18-crown-6, a new product was isolated as dark green needle-shaped crystals. The X-ray diffraction analysis confirmed the formation of a solvent-separated ion-pair with a Cs counterion, namely $[Cs^+(18\text{-crown-}6)_2][C_{39}H_{21}^-]$ (**Cs^+-1_r^-**) (Scheme 2). This product confirms that reaction with molecular oxygen provides a simple and attractive way to transform the relatively unstable polycyclic dianion radicals into closed-shell monoanions.

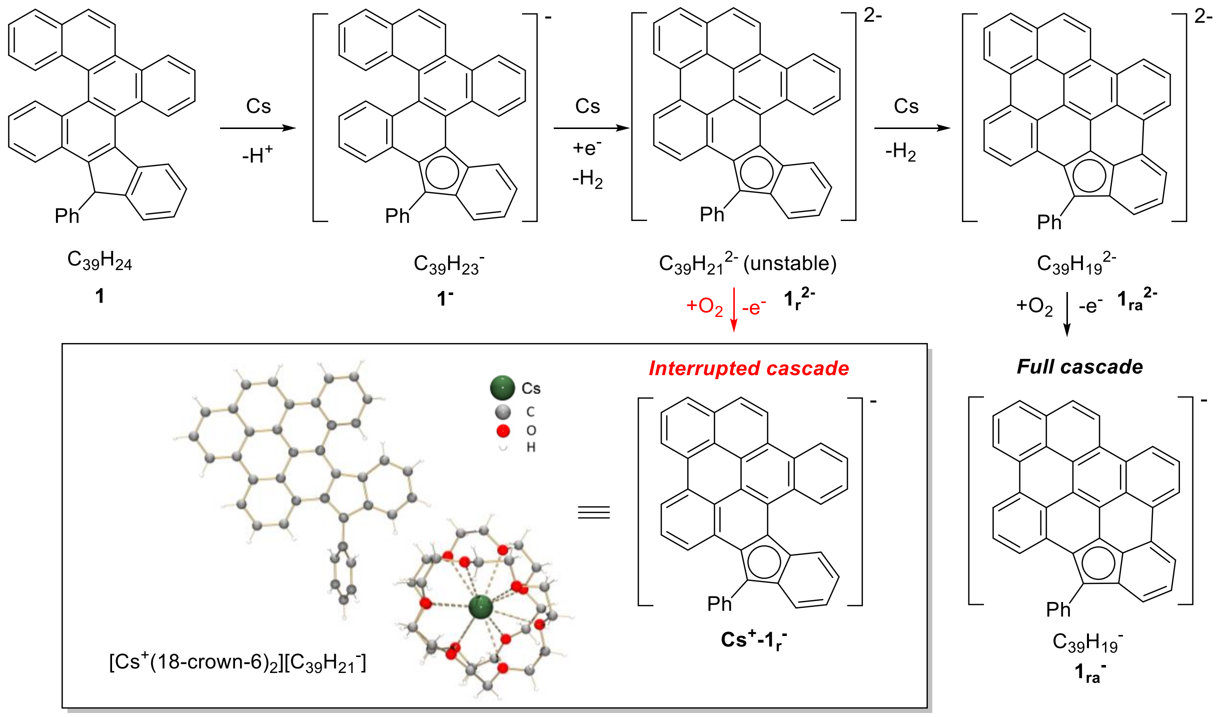

Scheme 2. Reaction sequence for the interaction of **1** with Cs metal with an added oxidation step that interrupts the bis-cyclization cascade.

Crystal structure and geometric features of the interrupted-cascade product. In the crystal structure of **Cs^+-1_r^-** (Figure 2), the Cs^+ ion is sandwiched by two 18-crown-6 ether molecules, with the Cs···O distances ranging from 3.219(13) to 3.445(15) Å.[102,17] The cationic $\{Cs^+(18\text{-crown-}6)_2\}$ moiety is solvent-separated from the **1_r^-** ($C_{39}H_{21}^-$) monoanion. It should be noted that the double helicene core of $\mathbf{1}^-$ ($C_{39}H_{23}^-$) was transformed to a new mono-helicene, $\mathbf{1_r}^{2-}$ ($C_{39}H_{21}^{2-}$), before turning into the planarized $\mathbf{1_{ra}}^{2-}$ ($C_{39}H_{19}^{2-}$) dianion with a new C13–C18 bond formed through reductive C−C coupling. This provides unique experimental evidence confirming the first (out of two) step in reductive C−C coupling reaction from $\mathbf{1}^-$ ($C_{39}H_{23}^-$) to $\mathbf{1_{ra}}^{2-}$ ($C_{39}H_{19}^{2-}$). Notably, this result is consistent with the previous computational study. In $\mathbf{1_r}^-$ ($C_{39}H_{21}^-$), the average bond angle on C7 is 120.0°, with the value being consistent with that observed in $\mathbf{1}^-$ ($C_{39}H_{23}^-$) (119.9°). The exocyclic C6–C7 bond (1.482(18) Å) is shorter in comparison with that in **1** (1.552(7) Å) (Table 1). Aromatization in the five-membered ring significantly shortens the C7–C8, and C7–C39 bonds in $\mathbf{1_r}^-$ ($C_{39}H_{21}^-$) (to 1.416(14) Å, 1.445(14) Å) in comparison to those bonds in the neutral precursor **1**. Interestingly, significant structural changes are not limited to the pentagonal unit. For example, the C16–C17 bond is shortened to 1.42(2) Å while the C14–C15 bond is elongated to 1.47(2) Å.

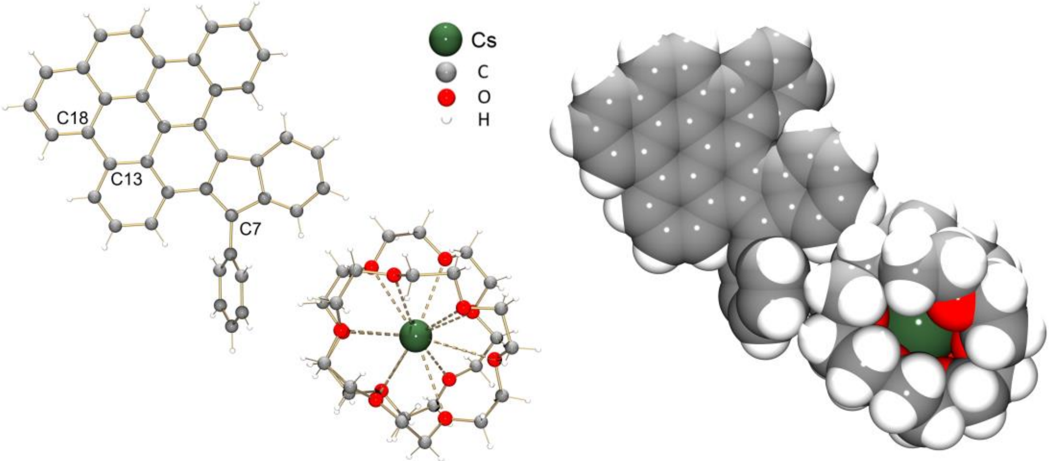

Figure 2. Crystal structure of [Cs^+(18-crown-6)$_2$][$C_{39}H_{21}^-$] ($\mathbf{Cs^+\text{-}1_r^-}$), ball-and-stick and space-filling models.

Table 1. Selected C–C bond length distances (Å) in $C_{39}H_{24}$, $C_{39}H_{23}^-$, and $C_{39}H_{21}^-$ along with a C-atom numbering scheme.

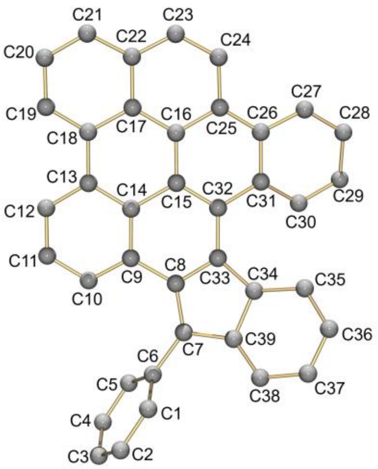

Bond	$C_{39}H_{24}$ (**1**)[35]	$C_{39}H_{23}^-$ ($\mathbf{1}^-$)[35*]	$C_{39}H_{21}^-$ ($\mathbf{1_r}^-$)
C6–C7	1.522(7)	1.465(14)	1.482(18)
C7–C8	1.510(7)	1.410(14)	1.422(17)
C7–C39	1.521(7)	1.432(14)	1.450(19)
C9–C14	1.417(7)	1.422(14)	1.438(18)
C14–C15	1.452(7)	1.463(14)	1.47(2)
C16–C17	1.452(7)	1.467(14)	1.42(2)
C13–C18	–	–	1.47(2)

[*] *Values are averaged.*

The distortion of the $C_{39}H_{21}^-$ core in $\mathbf{1_r}^-$ can be illustrated by selected torsion and dihedral angles (Table 2). Compared with the deprotonated $C_{39}H_{23}^-$ core, the single reductive C–C coupling allows the torsion and dihedral angles near the new ring J to become dramatically decreased ($|\text{torsion angle}|_{\text{avg.}} = 2.5°$, $\text{dihedral angle}_{\text{avg.}} = 24.8°$), with the values being close to those in $C_{39}H_{19}^{2-}$. In contrast, the corresponding torsion and dihedral angles near the ring G are mostly unchanged ($|\text{torsion angle}|_{\text{avg.}} = 20.1°$ vs 21.3°, $\text{dihedral angle}_{\text{avg.}} = 20.4°$).

Table 2. Selected torsion and dihedral angles (°) in $C_{39}H_{24}$, $C_{39}H_{23}^-$, and $C_{39}H_{21}^-$, along with an angle labeling scheme.

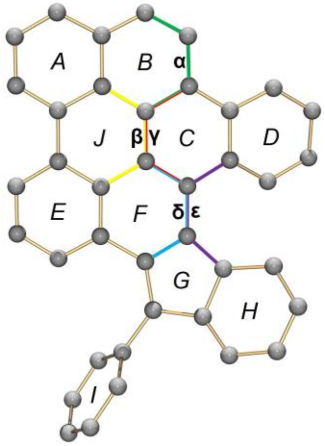

	Angle	$C_{39}H_{24}$ (**1**)[35]	$C_{39}H_{23}^{-}$ (**1**$^-$)[35*]	$C_{39}H_{21}^{-}$ (**1**$_r^-$)
|Torsion Angle|	***α***	2.2	0.5	0.9
	β	37.0	33.1	2.9
	γ	25.5	22.1	3.6
	δ	18.0	13.2	15.9
	ε	31.7	29.3	24.5
Dihedral Angle	A/G	51.4	42.7	25.2
	B/G	42.8	39.1	24.3
	D/G	38.8	40.1	35.5
	E/G	12.8	21.6	18.3
	H/G	5.6	3.3	7.4
	I/G	86.2	47.6	55.7

[*] *Values are averaged.*

In the solid-state structure of **Cs$^+$-1$_r^-$**, a 2D layer is formed through C–H$\cdots\pi$ interactions between the $C_{39}H_{21}^{-}$ monoanions and the adjacent 18-crown-6 ether molecules, with shortest distances ranging from 2.673(18) Å to 2.831(18) Å (Figure 3). No significant interactions were found between the adjacent layers.

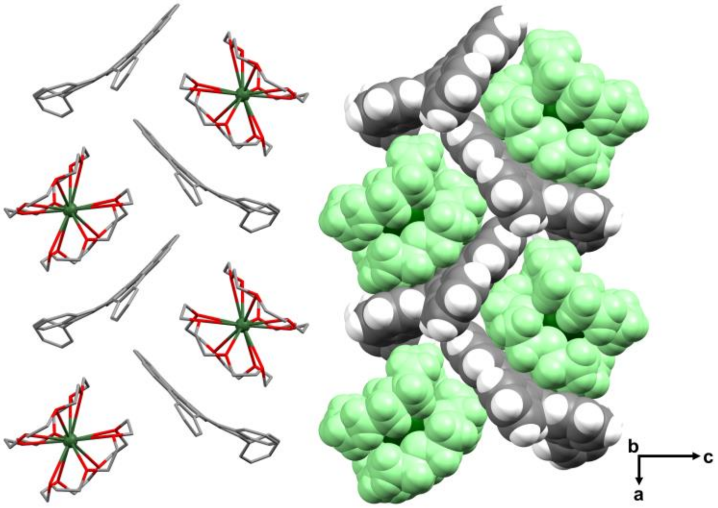

Figure 3. Solid state packing in **Cs$^+$-1$_r$$^-$**, mixed and space-filling models. {Cs$^+$(18-crown-6)$_2$} moieties are shown in green.

Reduction-induced cyclization of mono-helicene. Although the mono[5]helicene **2** ($C_{31}H_{20}$) is significantly less strained than bis-helicene **1** ($C_{39}H_{24}$, *vide infra* in the Computational section), it readily undergoes a similar transformation. The chemical reaction of the mono-helicene with K and Cs metals in THF proceeds through two distinctive steps, which can be monitored by UV-Vis spectroscopy (Figures S2–S4). The first step is accompanied by the appearance of a red-orange color with three major absorption bands centered at 327, 393, and 491 nm (for Cs reaction), which is slightly metal ion dependent. The reaction can be stopped at this stage and the resulting products have been isolated from both K- and Cs-induced reactions. Using slow diffusion of hexanes to the THF reaction solution, the K and Cs salts of the deprotonated monoanion of **2** were successfully crystallized in the presence of 18-crown-6 ether (Scheme 3). The single crystal X-ray diffraction analysis confirmed the formation of a solvent-separated ion-pair with Cs counterion, [Cs$^+$(18-crown-6)$_2$][$C_{31}H_{19}^-$] (**Cs$^+$-2$^-$**), and a contact ion-pair with K counterion, [{K$^+$(18-crown-6)}($C_{31}H_{19}^-$)] (**K$^+$-2$^-$**).

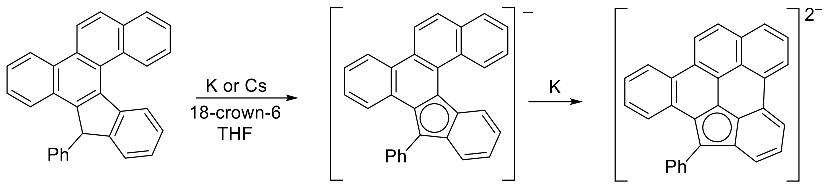

2

$[Cs^+(18\text{-crown-6})_2][C_{31}H_{19}^-]$
Cs^+-2^-
$[\{K^+(18\text{-crown-6})\}(C_{31}H_{19}^-)]$
K^+-2^-

$[\{K^+(18\text{-crown-6})\}_2(C_{31}H_{17}^{2-})]$
$(K^+)_2$-2_a^{2-}

Scheme 3. The two-step reaction sequence of mono-helicene **2** with alkali metals.

Upon further reduction, the color of the reaction mixture quickly changes from red-orange to deep brown, with a max absorption band centered at 339 nm (Figure S3). Using slow diffusion of hexanes into a THF reaction solution, a new product was crystallized in 55% yield from the K-induced reaction in the presence of 18-crown-6 ether. Based on single crystal X-ray diffraction analysis, it was confirmed to be $[\{K^+(18\text{-crown-6})\}_2(C_{31}H_{17}^{2-})]$ (**$(K^+)_2$-2_a^{2-}**). Notably, the core of the mono-helicene **2** was transformed *via* a reductive C–C coupling reaction to form a new $C_{31}H_{17}^{2-}$ dianion (**2_a^{2-}**). Remarkably, even the diminished polycyclic aromatic core of **2_a^{2-}** (seven rings – three fewer than in the decacyclic core of dianion **1_{ra}^{2-}**) is still capable of sustaining the two negative charges and the radical center of the cyclized dianion radical. The radical nature of the dianionic cyclic product was confirmed by its EPR spectrum (see Figure S15).

Crystal structures of the anionic and dianionic products from the mono-helicene reaction: In the crystal structure of **Cs^+-2^-** (Figure 4), the Cs^+ ion is fully wrapped by two crown ether molecules ($Cs\cdots O_{crown}$, 3.165(6)–3.495(6) Å) to afford the $\{Cs^+(18\text{-crown-6})_2\}$ cationic moiety that is solvent-separated from the anionic helicene core. This results in the formation of the first "naked" $C_{31}H_{19}^-$ monoanion which allows to monitor the helicene core geometry changes without metal binding influence. The proton on C7 is removed during the first step, which is similar to that observed for the previously reported bis-helicene **1**.[35] The proton removal on C7 can be confirmed by the disappearance of the peak at 5.41 ppm in the ^1H NMR spectrum. The average bond angle on C7 is increased from 109.6° (1) to 119.7° in **2^-**, which is indicative of the formation of a typical sp^2 hybridized C-atom. Meanwhile, the C6–C7 bond in **Cs^+-2^-** becomes shortened (1.473(5) Å) compared to that in **2** (1.527(3) Å), revealing increasing π-conjugation near the five-membered ring (Table 3). All Cs···O distances in **Cs^+-2^-** are close to those previously reported.[102,103]

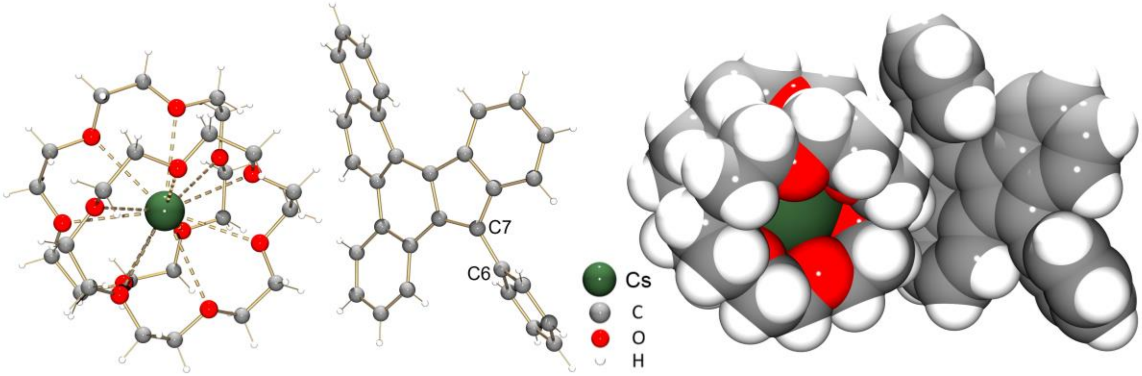

Figure 4. Crystal structure of $[Cs^{+}(18\text{-crown-}6)_2][C_{31}H_{19}^{-}]$ (**Cs⁺-2⁻**), ball-and-stick and space-filling models.

In contrast to **Cs^{+}-2^{-}**, the K^{+} counterion trapped by one 18-crown-6 molecule ($K\cdots O_{crown}$, 2.742(4)–2.841(5) Å) forms a contact ion-pair with the helicene monoanion in $[\{K^{+}(18\text{-crown-}6)\}(C_{31}H_{19}^{-})]$ (**K^{+}-2^{-}**). In the crystal structure of **K^{+}-2^{-}** (Figure 5), the average bond angle on C7 is 120.0°, with the value being consistent with that observed in **Cs^{+}-2^{-}** (119.7°). The C6–C7 bond is slightly shorter (1.467(7) Å) than that in **Cs^{+}-2^{-}**, but still in the range of an aromatic C–C bond (Table 1). The K^{+} ion binds to a six-membered ring of the $C_{31}H_{19}^{-}$ core in an η^{2}-mode with $K\cdots C$ distances of 3.138(7) Å and 3.234(7) Å. This coordination site is consistent with the molecular electrostatic potential map (MEP) of this system, which shows that the charge is localized on the 5-membered ring and its neighboring 6-membered ring (*vide infra*, Figure 11a). Notably, an extra $K\cdots C$ contact (3.304(5) Å) found between the K^{+} ion and the adjacent $C_{31}H_{19}^{-}$ monoanion results in the propagation of a one-dimensional polymeric chain in **K^{+}-2^{-}** (Figure 6). All $K\cdots C$ and $K\cdots O$ distances in **K^{+}-2^{-}** are comparable to the reported values.[104–106]

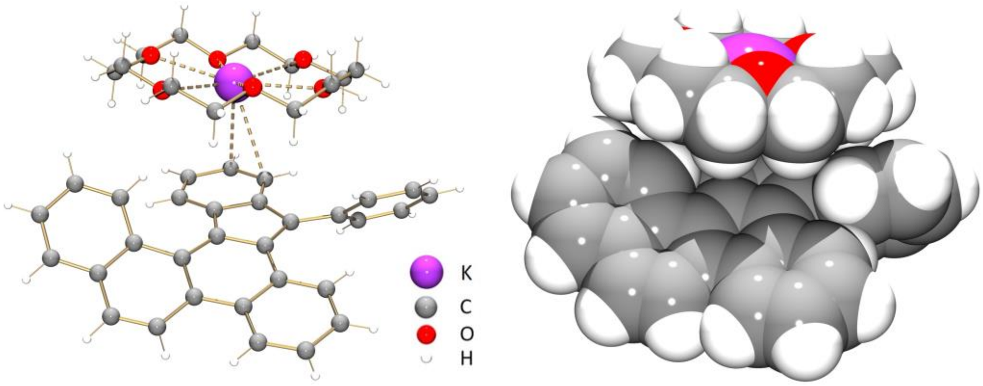

Figure 5. Crystal structure of $[\{K^+(18\text{-crown-6})\}(C_{31}H_{19}^-)]$ (**K^+-2$^-$**), ball-and-stick and space-filling models.

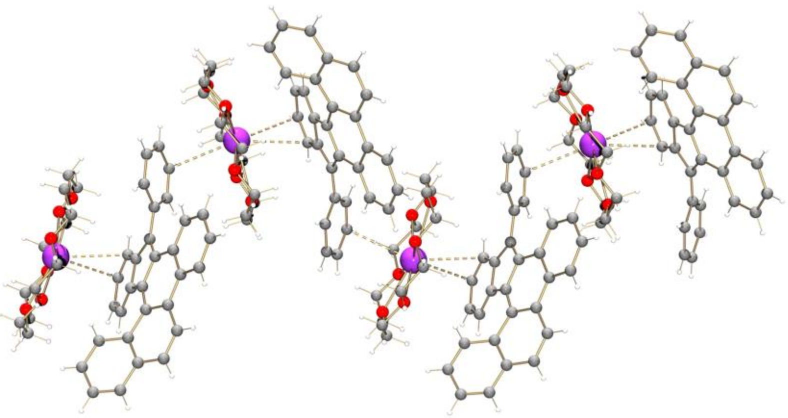

Figure 6. 1D polymeric chain of **K^+-2$^-$**, ball-and-stick model.

In the crystal structure of **$(K^+)_2$-2$_a^{2-}$** (Figure 7), the K1 ion binds to a six-membered ring of $C_{31}H_{17}^{2-}$ in an η^3-fashion (K···C, 3.084(4)–3.383(4) Å), while the K2 ion is η^3-coordinated to the adjacent five-membered ring (K···C, 3.057(4)–3.265(5) Å). The coordination environment of each K^+ ion is completed by one 18-crown-6 ether molecule, with corresponding K···O distances spanning over 2.755(4)–3.042(4) Å. All K···C and K···O distances are close to those previously reported.[104–106]

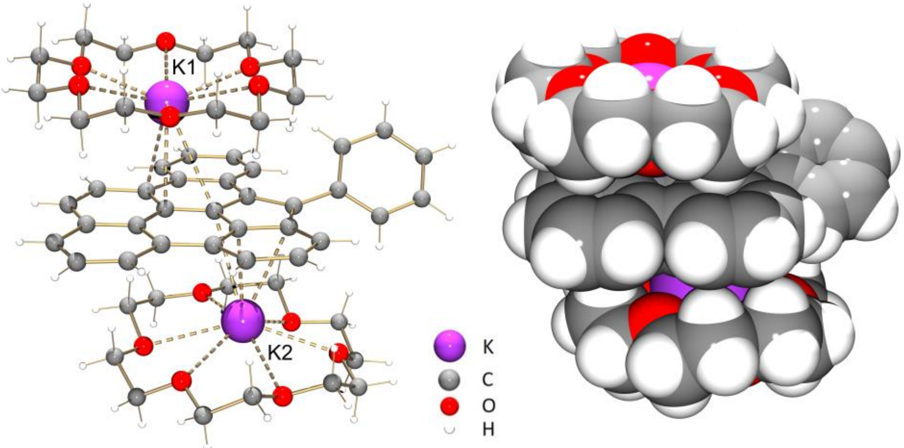

Figure 7. Crystal structure of $[\{K^+(18\text{-crown-6})\}_2(C_{31}H_{17}{}^{2-})]$ (**$(K^+)_2$-$2_a{}^{2-}$**), ball-and-stick model.

It should be noted that the dianion in **$(K^+)_2$-$2_a{}^{2-}$** becomes almost planar with the formation of a new C−C bond at C22–C27 (1.420(7) Å). Furthermore, the intramolecular strain caused by the ring closure results in C–C bond length alternation in the newly formed $C_{39}H_{17}{}^{2-}$ dianion. Compared to the helicene monoanion core, the bond lengths on the exterior of the framework (namely C7–C8, C7–C31, C9–C14, C16–C17, C19–C20, C21–C22, C27–C28, and C30–C31) become elongated by about 0.05 Å in **$(K^+)_2$-$2_a{}^{2-}$**, while those on the interior sites (C20–C21, C23–C24, C24–C25, and C25–C26) are shortened by about 0.03 Å (Table 3).

Table 3. Selected C–C bond length distances (Å) in **2, Cs^+-2^-, K^+-2^-, $(K^+)_2$-$2_a{}^{2-}$** along with C-atom numbering schemes.

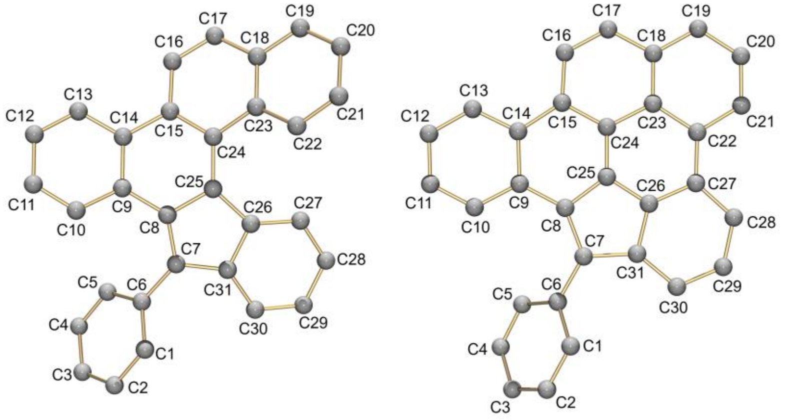

Bond	$C_{31}H_{20}$ (**2**)^{36} *	$C_{31}H_{19}{}^{-}$ (**Cs^+-2^-**)	$C_{31}H_{19}{}^{-}$ (**K^+-2^-**)	$C_{31}H_{17}{}^{2-}$ (**$(K^+)_2$-$2_a{}^{2-}$**)

C6–C7	1.527(3)	1.473(5)	1.467(7)	1.461(6)
C7–C8	1.522(3)	1.402(5)	1.434(8)	1.444(6)
C7–C31	1.520(3)	1.430(5)	1.407(8)	1.471(6)
C9–C14	1.431(3)	1.420(6)	1.423(7)	1.464(7)
C16–C17	1.367(3)	1.366(6)	1.341(7)	1.423(7)
C19–C20	1.385(4)	1.362(6)	1.349(8)	1.419(6)
C21–C22	1.391(3)	1.372(6)	1.367(9)	1.443(7)
C27–C28	1.402(3)	1.371(6)	1.370(8)	1.415(7)
C30–C31	1.384(3)	1.404(5)	1.406(8)	1.425(6)
C22–C27	–	–	–	1.420(7)

*Values are averaged.

The distortion of the carbon framework during deprotonation and reduction steps was analyzed using selected torsion and dihedral angles (Table 4). After the site-selective deprotonation, the torsion and dihedral angles of $C_{31}H_{19}^{-}$ in **Cs^{+}-2^{-}** and **K^{+}-2^{-}** remain unchanged compared with those in **2**, except a decrease in value of ~36° in the dihedral angle ∠G/E. Upon reductive C–C coupling, all angles of $C_{31}H_{17}^{2-}$ in **(K^{+})$_2$-2^{2-}** become dramatically decreased (for torsion angles up to 0.6–2.6°; for dihedral angles up to 2.6–5.6°, except the external ∠G/E angle), clearly indicating the ligand core planarization.

Table 4. Selected torsion and dihedral angles (°) in **2, Cs^{+}-2^{-}, K^{+}-2^{-}, (K^{+})$_2$-2^{2-}** along with a labeling scheme.

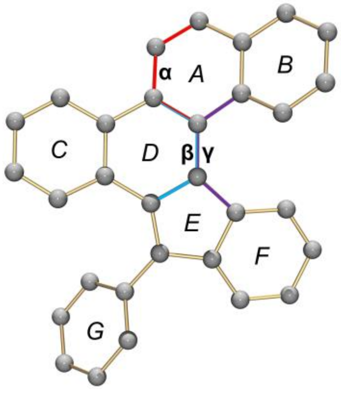

	Angle	$C_{31}H_{20}$ **(2)**^{36} *	$C_{31}H_{19}^{-}$ **(Cs^{+}-2^{-})**	$C_{31}H_{19}^{-}$ **(K^{+}-2^{-})**	$C_{31}H_{17}^{2-}$ **((K^{+})$_2$-2$_a$$^{2-}$)**
|Torsion Angle|	***α***	4.0	3.0	3.7	2.6
	β	16.4	12.6	14.8	0.6
	γ	20.4	24.3	24.7	0.7
	B/E	31.9	37.9	37.3	2.6

Dihedral Angle	C/E	9.4	19.6	12.5	5.6
	F/E	5.9	6.3	6.7	4.1
	G/E	85.4	48.9	49.3	42.7

[*] *Values are averaged.*

In the solid-state structure of **Cs$^+$-2$^-$**, a 3D network is formed through multiple C–H···π interactions between the $C_{31}H_{19}^-$ monoanions and the adjacent 18-crown-6 ether of the cationic moieties, with distances ranging from 2.605(5) Å to 2.809(5) Å (Figure 8). In the solid-state structure of **K$^+$-2$^-$**, a 1D polymeric chain is formed due to the intermolecular K···C contacts (3.304(5) Å) between the K$^+$ ions and the adjacent $C_{31}H_{19}^-$ monoanions (Figure 6). The 1D columns are further linked into a 2D layer through C–H···π interactions between the monoanions and the 18-crown-6 ether molecules from adjacent columns with the distance measured at 2.728(8) Å (Figure 9).

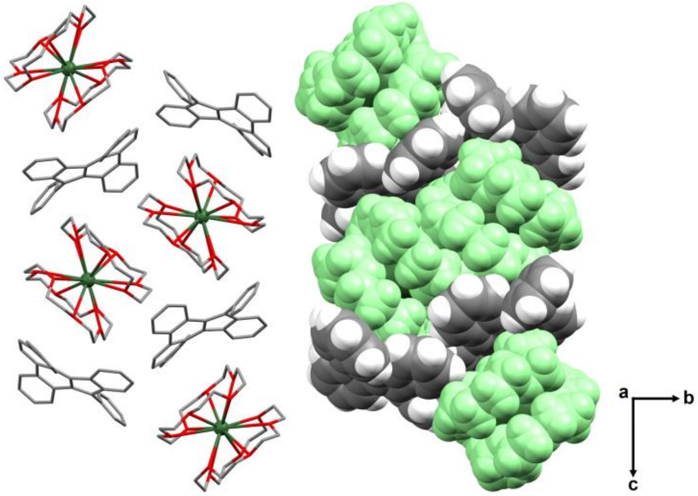

Figure 8. Solid-state packing in **Cs$^+$-2$^-$**, mixed and space-filling models. {Cs$^+$(18-crown-6)$_2$} moieties are shown in green.

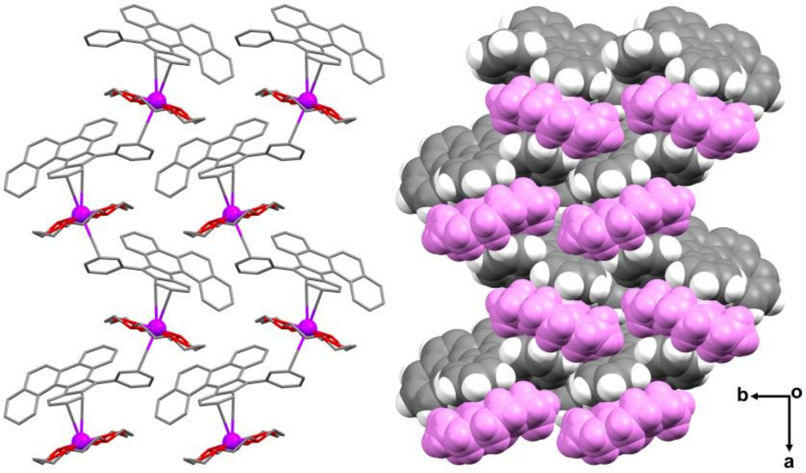

Figure 9. Solid-state packing in **K^+-2^-**, mixed and space-filling models. {K^+(18-crown-6)} moieties are shown in purple.

In the solid-state structure of **$(K^+)_2$-2_a^{2-}**, unlike the previously reported **1_{ra}^{2-}** ($C_{39}H_{19}^{2-}$) dianion, which formed a solvent-separated ion-triplet with two Cs counterions, the two coordinated {K^+(18-crown-6)} moieties prevent the formation of strong interactions between the molecules (Figure 10).[35]

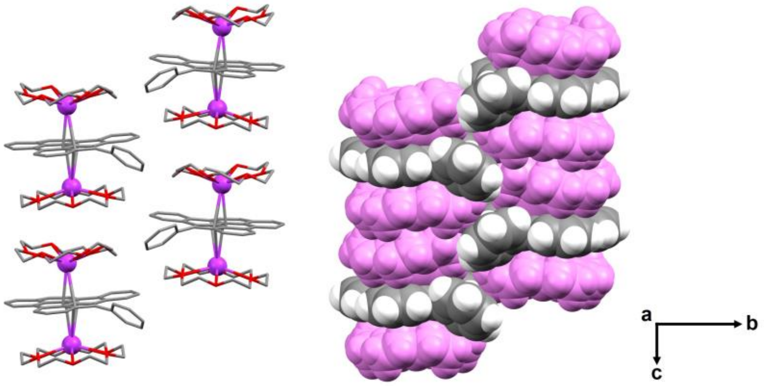

Figure 10. Solid-state packing in **$(K^+)_2$-2_a^{2-}**, mixed and space-filling models. {K^+(18-crown-6)} moieties are shown in purple.

Computational Analysis

To obtain a better understanding of the transformation pathway of the mono-helicene case and the effects governing it, we conducted a computational study. Two main perspectives were investigated: a) the sequence of steps to achieve the product, and b) the three main effects driving the reaction, namely, charge delocalization, aromaticity, and helical strain. Throughout our analysis of both of these aspects, we also draw comparisons between the mono-helicene and the previously reported bis-helicene.

Reaction pathway. The overall reaction involves deprotonation, reduction, cyclization, and formal loss of H_2 to form dianion $\mathbf{2_a^{2-}}$ containing the fused, planar heptacyclic structure. The first step in the pathway is unambiguous, i.e., deprotonation to afford monoanion $\mathbf{2^-}$. In principle, two sequences are possible after deprotonation: a) cyclization followed by reduction or b) reduction followed by cyclization. Scheme 4a depicts these two conceivable pathways and their respective intermediates (denoted as $\mathbf{2_{aH2}^-}$, $\mathbf{2_a^-}$, $\mathbf{2^{2-}}$, and $\mathbf{2_{aH2}^{2-}}$, respectively).

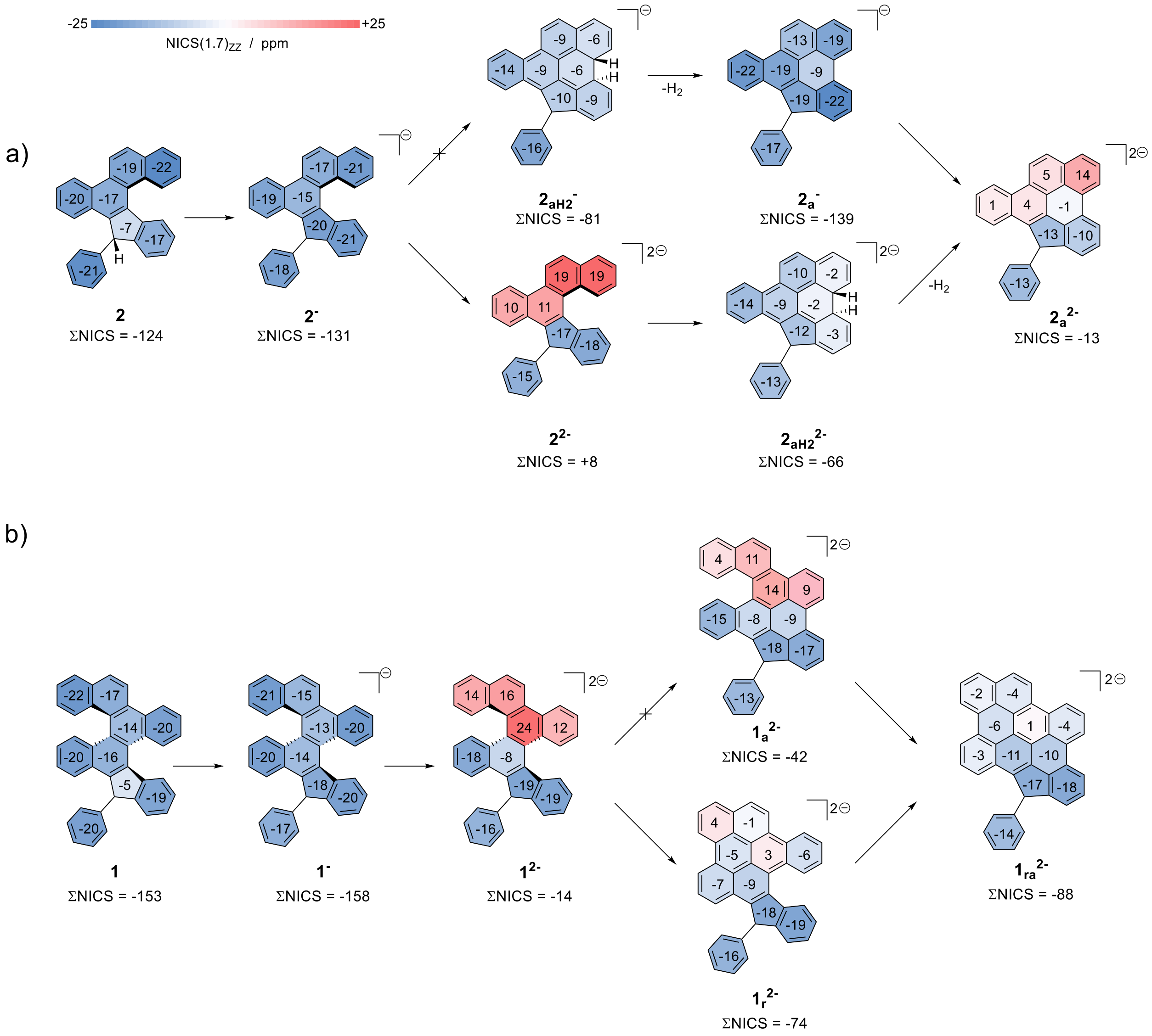

Scheme 4. a) The two possible pathways from **2** to $\mathbf{2_a}^{2-}$. Upper route: cyclization before reduction; Bottom route: reduction before cyclization. b) The cyclization pathway of the bishelicene species. Upper route: adjacent cyclization first; Bottom route: remote cyclization first. NICS(1.7)$_{ZZ}$ values are reported for each ring in ppm and are rounded to the nearest integer. Ring-fill colors indicate magnetic character: blue = diatropic (aromatic), red = paratropic (antiaromatic). Color intensity is proportional to the magnitude of the NICS(1.7)$_{ZZ}$ value; bar is shown in bottom left-hand corner.

Our computational results indicate that the operative pathway is the bottom route shown in Scheme 4a: deprotonation followed by reduction, cyclization, and finally extrusion of H_2 (i.e., the “Reduction-first” route). This conclusion is supported by three individual pieces of evidence. First, a transition state (TS) was located for the cyclization process of $\mathbf{2}^{2-}$ à $\mathbf{2}_{\mathbf{aH2}}^{2-}$, whereas an analogous TS could not be located for cyclization of $\mathbf{2}^{-}$ to $\mathbf{2}_{\mathbf{aH2}}^{-}$ (See SI for further details). Second, visual inspection of the lowest unoccupied molecular orbital (LUMO) of $\mathbf{2}^{-}$ reveals a constructive overlap between the two carbons that will bond in the cyclization event (Figure S25 in the SI). Hence, population of this orbital by injection of an additional electron in the reduction step would promote the cyclization step, and this orbital would become the singly-occupied MO (SOMO) of $\mathbf{2}^{2-}$ (Figure 11b, left). Third, the difference in electronic energy between $\mathbf{2}^{2-}$ and $\mathbf{2}_{\mathbf{aH2}}^{2-}$ is ~29 kcal/mol, whereas between $\mathbf{2}^{-}$ and $\mathbf{2}_{\mathbf{aH2}}^{-}$ it is ~57 kcal/mol. Though these energies neglect solvation and counter-ion effects, the large difference between the two options suggests that the cyclization from $\mathbf{2}^{2-}$ is more likely.

Interestingly, the antiaromatic hotspot is moved further away from the cyclopentadienyl moiety in the dianion formed from the bishelicene species (Scheme 4b). Remarkably, this larger system still shows localization of antiaromatic character after electron injection as well as the subsequent relief of antiaromaticity associated with the cyclization. Note that the experimentally observed path (via $\mathbf{1}_{\mathbf{r}}^{2-}$) dissipates the antiaromatic region sooner than the alternative path (via $\mathbf{1}_{\mathbf{a}}^{2-}$). The full description of the two possible pathways for the bishelicene is shown in the Supporting Information, Figure S24.

Homodesmotic equations for the mono-helical system further support that the cyclization becomes energetically more favorable, by about 5 kcal/mol, after injection of the second charge (Scheme 5b). We note that this was also the conclusion in the case of the bis-helical system,[35] where we found that the reduction preceded the first cyclization step.

Scheme 5 also illustrates that the thermodynamic driving force for the cyclization of mono-helicene is considerably (~20 kcal/mol) lower than for the full cyclization of bis-helicene, in a good agreement with the relative strain content in these two systems. In this context, the experimental observation of mono-helicene cyclization becomes especially significant as it expands the scope of this new reductive cyclization process to considerably less strained systems.

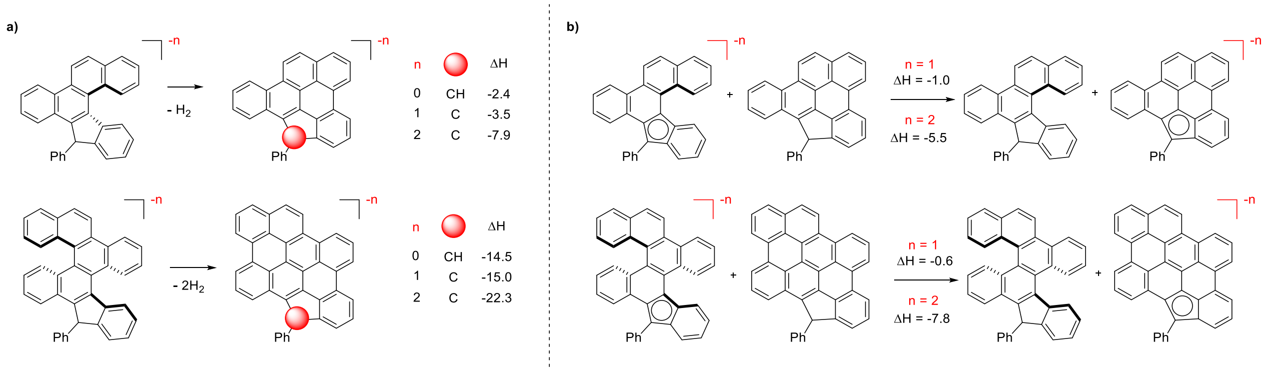

Scheme 5. a) The overall ΔH for the mono-helicene and bis-helicene cyclization(s) in the three charge states (neutral, mono-, and di-anionic). b) Homodesmotic equations for the comparison of the effect of charge on the pathway thermodynamics.

Having determined the series of steps of the overall transformation for the mono-helicene cyclization, we now analyze this pathway through each of the three lenses described above: charge delocalization, aromaticity, and strain relief.

a. *Charge delocalization*. Upon deprotonation, the negative charge of monoanion **2**$^-$ is mostly centered on the 10-π electron circuit made up of the pentagonal unit and its neighboring benzene, as shown in the molecular electrostatic potential (MEP) maps in Figure 11a.

In the following reduction step, the new charge is distributed along the "top" four rings (rings *A*−*D*, as denoted in Table 2) of the compound, which corresponds to the spatial extent of the SOMO of this system (Figure 11b, left). Overall, it appears that the total −2 charge is distributed rather evenly over the hexacyclic core of **2**$^{2-}$. The subsequent cyclization step does not seem to impede delocalization; the MEP map of $\mathbf{2}_{\mathbf{aH2}}^{2-}$ shows that the charge continues to be delocalized, despite formal breaking of the conjugation in two of the rings (rings *B* and *F*). This can be explained by the hyperconjugation of the CH orbitals into the π-system, which affords continued delocalization (Figure 11b, right). Further support that that cyclization does not hinder delocalization is provided by a homodesmotic equation (Scheme S26 in the Supporting Information) indicating that the double negative charge is stabilized by the cyclization. Finally, extrusion of H_2 results in a fully conjugated and planar fused scaffold, over which the charge is distributed.

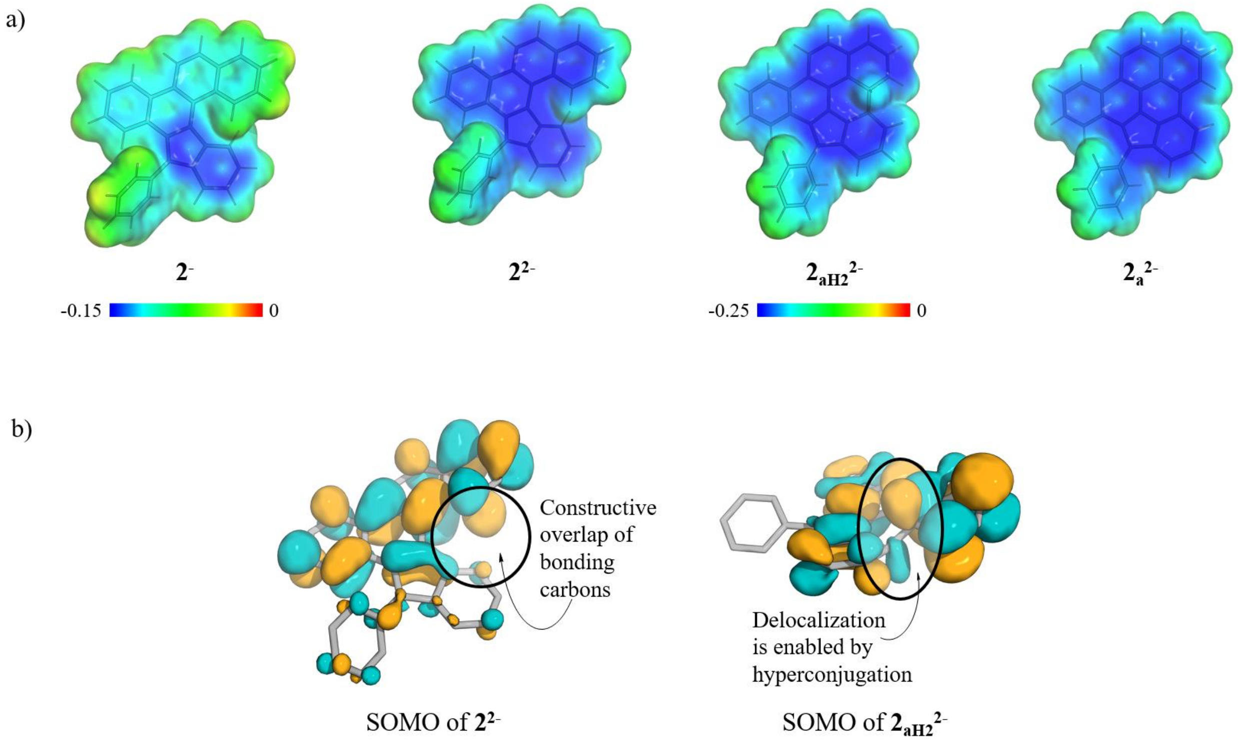

Figure 11. a) Molecular electrostatic potential maps for $\mathbf{2}^{-}$, $\mathbf{2}^{2-}$, $\mathbf{2}_{\mathbf{aH2}}^{2-}$, and $\mathbf{2}_{\mathbf{a}}^{2-}$. The maps are plotted at the isosurface value $\alpha = 0.005$. For the monoanionic $\mathbf{2}^{-}$, the range is from [-0.15,0], for the dianionic compounds $\mathbf{2}^{2-}$, $\mathbf{2}_{\mathbf{aH2}}^{2-}$, and $\mathbf{2}_{\mathbf{a}}^{2-}$, the range is [-0.25,0]. b) Singly-occupied molecular orbitals (SOMOs) and their respective interactions for (left) $\mathbf{2}^{2-}$ and (right) $\mathbf{2}_{\mathbf{aH2}}^{2-}$. The orbitals are plotted at the isosurface value $\alpha = 0.02$.

b. Aromaticity. The aromaticity of the various intermediates was evaluated using the NICS(1.7)$_{ZZ}$ metric[107–109] and was visualized for the final cyclization products using the NICS2BC method (Figure 12).[110] Scheme 4 details the values for each ring, as well as ΣNICS(1.7)$_{ZZ}$ values for each system, which we use as a qualitative indicator for overall gain/loss of aromatic character. We observe that the initial deprotonation step results in a gain of aromatic character in the pentagonal moiety, due to the formation of a 10 π-electron bicyclic subunit containing the five-membered ring and its neighboring six-membered ring (rings *E* and *F*; this is supported by the MEP map of $\mathbf{2}^{-}$ in Figure 11, which shows charge delocalization over both rings). Overall, the aromatic character of the system is slightly increased (ΣNICS(1.7)$_{ZZ}$ = -131 ppm, compared to -124 ppm in the neutral parent).

The subsequent reduction step to afford $\mathbf{2}^{2-}$ creates a split in the system, whereby the "top" four rings (rings *A*−*D*) have markedly paratropic chemical shifts (positive NICS(1.7)$_{ZZ}$ values, see Scheme 4), indicating antiaromatic character, while the bottom part of the system (rings *E*, *F*, and pendant ring *G*) retains its diatropicity (i.e., aromatic in nature). The area of paratropicity corresponds to the spatial extent of the SOMO (Figure 11b left), which is in line with the expectation that the newly populated orbital will be the source of any new—in this case paratropic—magnetic contributions. Overall, the aromatic character of the system changes substantially (ΣNICS(1.7)$_{ZZ}$ = +8 ppm). These observations echo the same behavior that was observed for the bis-helical structure (Scheme 4b), in which charge injection leads to the formation of two distinct regions with opposite aromatic character, and antiaromatic behavior corresponds to the spatial extent of the SOMO (shown also in Reference [35] and in the SI).

The following cyclization step results in significant relief of antiaromaticity (ΣNICS(1.7)$_{ZZ}$ = -66 ppm for $\mathbf{2}_{\mathbf{aH2}}^{2-}$). Note that the three most right-side rings of $\mathbf{2}_{\mathbf{aH2}}^{2-}$ (and $\mathbf{2}_{\mathbf{a}}^{-}$) are, in principle, not fully conjugated and their calculated NICS(1.7)$_{ZZ}$ value should therefore not really be interpreted as a direct measure of aromaticity. However, our consideration of FMOs and MEP maps suggests a high degree of delocalization even over these non-fully-conjugated rings, rendering the evaluation of their magnetic behavior still worthwhile. Thus, we report these values for the sake of completeness and have included them in the calculation of the ΣNICS(1.7)$_{ZZ}$ for these molecules.

The final step, formal loss of H_2, reintroduces a split aromatic character in the fused system, which is seen clearly in the NICS2BC plot (Figure 12a): ring *B* is the only ring with marked antiaromaticity; rings *A*, *C*, *D*, and the newly formed ring are essentially non-aromatic, with no discernable ring currents; rings *E* and *F* are moderately aromatic. Pendant ring *G* is also aromatic (according to a separate calculation; NICS2BC plots are not representative for this ring, as it is not in the same plane as the rest of the system). Interestingly, this is somewhat different from the bis-helicene cyclization. For $\mathbf{1}_{\mathbf{ra}}^{2-}$, the aromatic section of the molecule encompasses four rings, and the remaining rings are essentially non-aromatic; there is no anti-aromatic region in the final cyclization product (Scheme 4b and Figure 12b).

Overall, we conclude that the injection of the electron jump-starts the operative reductive cyclization, by creating the high-energy dianionic antiaromatic intermediate $\mathbf{2}^{2-}$. The antiaromaticity of $\mathbf{2}^{2-}$ is likely the cause for the reduced barrier to cyclization, thus the relief of antiaromaticity drives the cyclization and loss of H_2 forward, similar to the bis-helical case. In contrast, the hypothetical "Cyclization-first" pathway does not introduce antiaromaticity; all of the intermediates are aromatic (Scheme 4) and thus the driving force of relieving antiaromaticity is not generated.

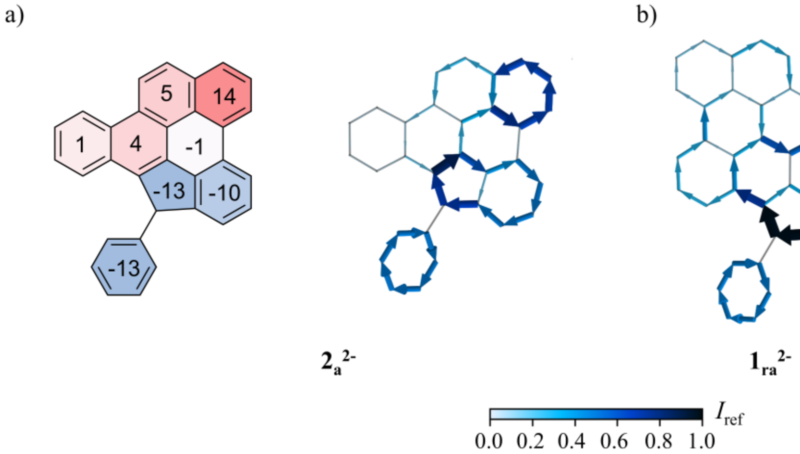

Figure 12. a) NICS(1.7)$_{ZZ}$ values and NICS2BC plot for $\mathbf{2}_{\mathbf{a}}^{2-}$ and b) NICS2BC plot for $\mathbf{1}_{\mathbf{ar}}^{2-}$. I_{ref} is with respect to benzene calculated at the same level of theory. The magnetic field is along the Z-axis, i.e., perpendicular to the plane of the page and pointing towards the reader; clockwise rotation indicates diatropic ring currents; counterclockwise rotations indicated paratropic ring currents.

b. *Strain*. To evaluate the magnitude of helical strain involved in the transformation, we studied three pentacyclic negatively charged isomers containing a five-membered ring. The charge of the systems is the same and the aromaticity is very similar (see NICS(1.7)$_{ZZ}$ values in Scheme 6), thus the differences in energies are likely due to the variations in strain. As the calculations show, the helical strain results in destabilization of ~6 kcal/mol, the relief of which contributes to the driving force.

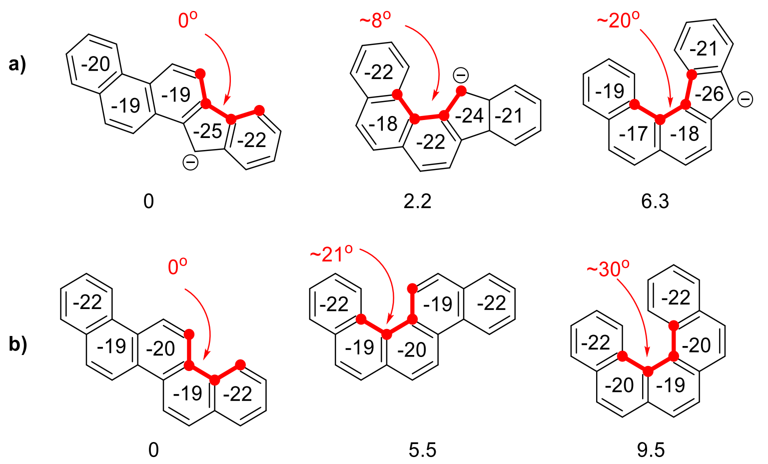

Scheme 6. Comparison of relative electronic energy of three isomeric forms with different dihedral angles for a) containing a cyclopentadienyl anion unit and b) containing only benzenoid units. Relative energy is given in kcal/mol. $\mathrm{NICS}(1.7)_{ZZ}$ values are reported for each ring in ppm and rounded to the nearest integer. Calculated at the B3LYP/6-311G(d,p) level.

To understand how the effect of strain differs between the two systems, we compare the cyclization event in the mono-helicene to each of the cyclization events in the bis-helicene, beginning with the first cyclization event. We previously performed an analogous isomer comparison using polybenzenoid pentacyclic structures to analyze the bis-helical cyclization.[35] Due to the geometry of the five-membered ring, the dihedral angles seen in the mono-helicene are smaller than in the polybenzenoid series (~8° and ~21°, compared to ~20°, and ~30°, respectively) and the strain energy is decreased (2.2 and 6.3 kcal/mol, compared to 5.5 and 9.5 kcal/mol relative energy, respectively). In other words, the relief of helical strain is expected to play a smaller role in driving the mono-helicene cyclization pathway than it does in the first cyclization of the bis-helical case.

In addition, we note that, similarly to the first cyclization step in the bis-helicene, the cyclization step in the mono-helicene is endergonic (ΔE = ~29 kcal/mol for the mono-helicene; ΔE = ~20 kcal/mol for the bis-helicene)). The fact that this step is uphill energetically, despite the remarkable loss of antiaromaticity, the potential gain in electron delocalization, and the loss of helical strain that accompany it, suggests that new sources of destabilization are generated. We attribute these to strain originating from: a) the tertiary carbons being forced into planarity by the new bond between them and b) the forced planarization around the five-membered ring (five-membered rings generally induce curvature, e.g., corannulene). Whereas the former is also experienced in the first cyclization of the bis-helicene (and is relieved by subsequent loss of H_2), the latter is not. This may account for part of the difference in energetic cost between the mono- and bis-helical systems.

Comparison to the second cyclization step in the bis-helicene highlights the importance of antiaromaticity relief as a driving force for a chemical transformation.[111–116] In this comparison, the structural aspects are similar: both involve the pentagonal unit. However, the second cyclization in bis-helicene[35] is ~11 kcal/mol more endothermic than the cyclization of mono-helicene. This difference can be rationalized by the observation that the mono-helicene cyclization couples relief of antiaromaticity to the cyclization event, while the bis-helicene has already exhausted this driving force when it reaches the second cyclization step.

In summary, the computational results allow us to ascertain the series of steps in the overall pathway, as well as evaluate the importance of the three main effects involved in the transformation. We find that the cyclization occurs following the reduction event, in which injection of charge forms the high-energy antiaromatic dianion $\mathbf{2}^{2-}$ (Scheme 4). Relief of the localized antiaromaticity and potential increase in charge delocalization mitigate the cost of the cyclization event, driving the reaction forward, even though the final product, $\mathbf{2_a}^{2-}$, does not regain the aromatic character of $\mathbf{2}^{-}$. Compared to the bis-helicene, the helical strain in the mono-helicene is lower and therefore its relief plays a smaller role in driving the reaction forward.

Computational Methods

All of the calculations reported herein were performed with the Gaussian 09 suite of programs, Version D.01.[117] The structures were optimized using the B3LYP[118,119] functional in conjunction with the 6-311G(d,p)[120,121] basis set and Grimme's D3[122,123] empirical dispersion correction (see Supporting Information for further details on choice of method and benchmarking). Structures were verified to be stationary points on the potential energy surface (i.e., $N_{imag} = 0$ for intermediates and $N_{imag} = 1$ for transition states). Note that the thermochemical properties were calculated in the gas phase at 298.15 K. Neither implicit solvent models nor the effects of other components of the reaction system (such as the reductant or counter-ions) were considered. Therefore, all values should be interpreted only inasmuch as the trends they reflect and only with respect to the changes incurred on the aromatic moiety. The values do not represent an accurate reflection of the overall thermodynamic profile of the reaction.

The Aroma program[124–127] was used to generate input files for nucleus-independent chemical shift (NICS)[107,128,109] calculations, which were performed using the gauge-including atomic orbitals (GIAO)[129,130] method at the same level of theory described above. The NICS(1.7)$_{zz}$ metric was chosen, based on the recommendation by Gershoni-Poranne and Stanger,[109,124] and these values are reported in ppm units throughout the text. The BC-Wizard program version 1.0[131] was used to generate the NICS2BC plots[110] (these were generated only for the final products because this method is only recommended for use with planar or close-to-planar molecules). Visualization of the molecular orbitals and electrostatic potential maps was done with PyMol version 2.5.2.[132] Sample input files are provided in the Supporting Information.

Conclusions

In conclusion, both bis-helicene **1** and mono-helicene **2** can undergo dehydrogenative ring-closure upon treatment with potassium or cesium metals. For the bis-helicene, the cyclization cascade can be interrupted after the first annulation. In both cases, localized antiaromatic character is generated by the injection of the second charge, and it is the relief of this destabilizing effect that acts as a driving force for the subsequent cyclization event. Importantly, in the bis-helicene, the location of the antiaromaticity determines the regioselectivity of the first cyclization.

The combination of experimental observations agrees well with the computational analysis. Together, experiments and theory suggest that the observed reactions start with deprotonation of the acidic C-H bond of the cyclopentadienyl moiety, followed by one-electron reduction, and finally the (sequence of) cyclization(s) (Scheme 7). The calculated thermodynamics of the ring closure show that cyclization prior to reduction is unlikely, as this process is significantly more uphill for the monoanionic pathway in comparison to the dianionic pathway. Furthermore, a relatively low-energy transition state for the cyclization of the dianion could be found, while the analogous monoanionic transition state remained elusive.

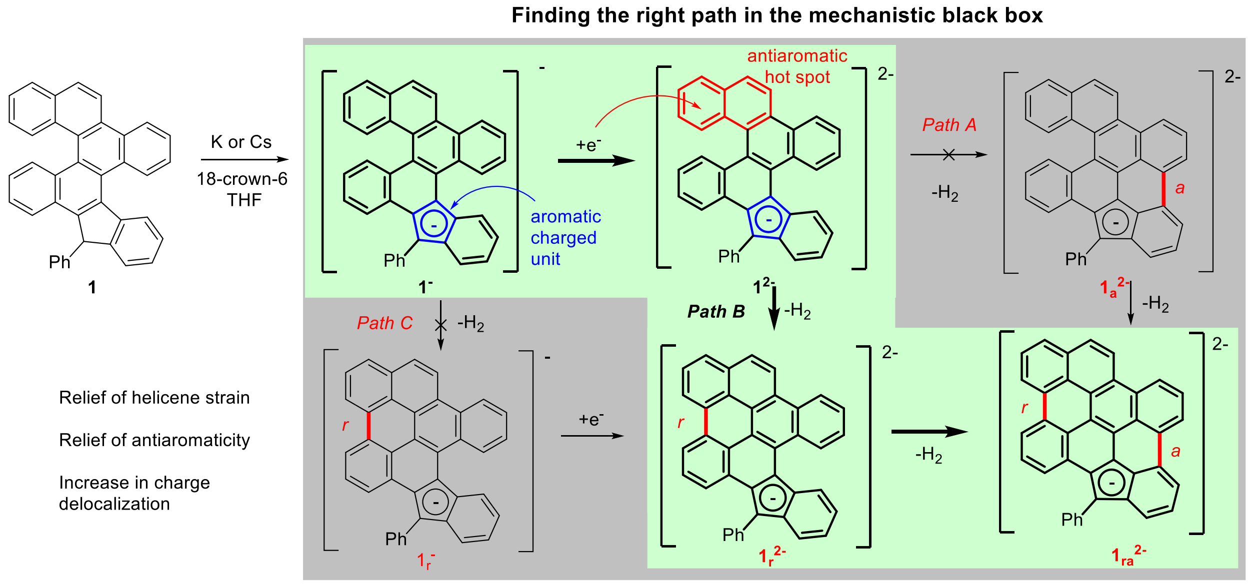

Scheme 7. The regioselectivity of the initial ring closure of the double cyclization sequence highlights the preferred path in the maze of mechanistic scenarios. The preferred path is shown in green.

As the computations show, the contribution of helical strain in promoting the C-C bond formation is smaller in the mono-helical system than it was in the bis-helical system. While it is still an important contributor to the driving force of the overall reaction, other factors may play bigger roles in the mono-helicene where smaller distortion is observed in comparison to the bis-helicene. Similarly, calculated molecular electrostatic potential maps (MEP maps) of the mono- and dianionic species suggest that, although improved charge delocalization is certainly a contributor to the overall driving force of the reaction from **2** to $\mathbf{2_a}^{2-}$, there are no dramatic changes in charge delocalization for the individual reaction steps along the reaction pathways.

Unlike the bis-helicene, where all three factors were closely responsible for the overall driving force, the calculated NICS(1.7)$_{ZZ}$ values and thermodynamic parameters suggest that release of antiaromaticity is the key component of the driving force for the cyclization of mono-helicene dianion. This can be understood in the following way: the cyclization step is energetically costly, as it introduces new types of strain into the molecules. We suggest that the destabilization gained by "pumping" in an additional electron into the respective mono-anion and forming the antiaromatic dianion is needed to overcome the barrier of the endothermic cyclization step. Thus, this transformation is only possible when the cost is mitigated by coupling it to the substantial energetic gain of antiaromaticity relief.

Indeed, the 2nd cyclization (i.e., reaction in the vicinity of the pentagonal unit) for the bis-helicene cascade is considerably less favorable than the 1st cyclization, because the antiaromaticity of the molecule has been “expended” and can no longer be used as a driving force. Further, the cyclization of the mono-helicene is less thermodynamically uphill than that of the helical portion containing the pentagonal unit in the bis-helicene. This observation further illustrates the effect of antiaromatic destabilization on local reactivity around the pentagonal unit. Cyclization at this region only alleviates antiaromaticity if it occurs as the first step, i.e., starts with the dianion of the precursor helicene. Finally, the formal loss of H_2 with the restoration of full cyclic conjugation is the closing step in both the mono- and the bis-cyclization pathways that renders these reactions exergonic.

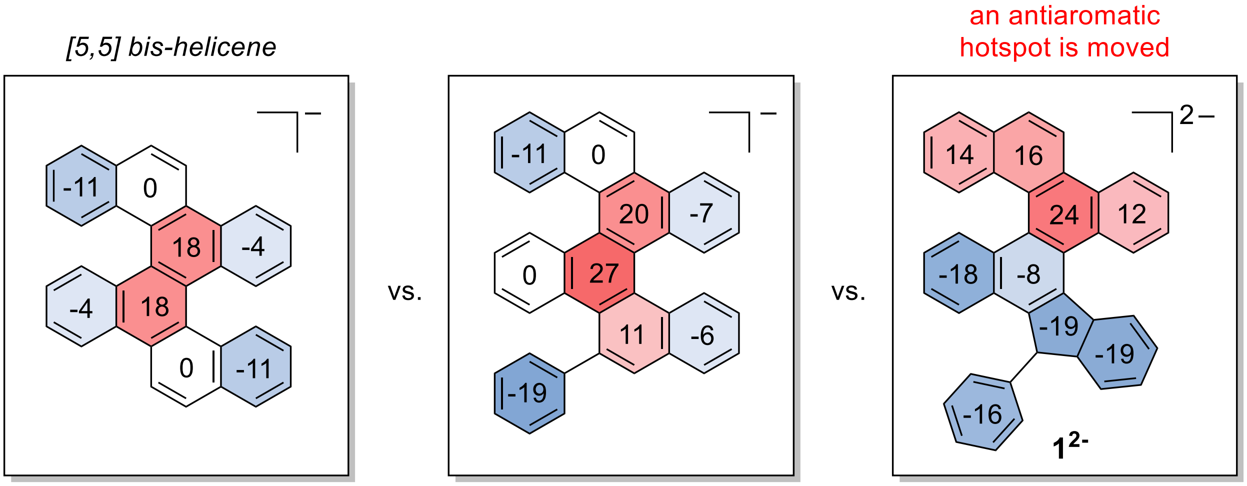

Figure 13. Contrasting patterns of local antiaromaticity in the parent [5,5] bis-helicene and its modified versions.

The effect of the pre-existing anionic center on the charge injected into the conjugated pi-system is illustrated in Figure 13. In the radical-anion derived from the parent [5,5] bis-helicene, the antiaromatic region is located at the center of the fused ring system, on the trigonally-annulated rings. Introduction of a pendant phenyl group relieves the symmetry and perturbs the electron density, such that the antiaromatic character extends to an adjacent ring; however, the antiaromatic character is still located at the center. Clearly, the situation changes in the helicene containing the anionic five-membered ring. A different pattern of antiaromaticity is created by the electrostatic directing effect of the first negative charge (located in the embedded cyclopentadienyl ring) on the second negative charge (introduced by the one-electron reduction that injects the additional electron in the π*-system of the helicene mono-anion). As the negative charges avoid each other, the second electron is forced to occupy a localized remote position in the polycyclic system. This location serves as a hotspot, the starting point for the cyclization cascade.

An intriguing conclusion from our observation is the emergence of the concept of localized antiaromaticity. The ability of confining aromaticity to a part of a conjugated π-system may provide a key to facilitating difficult transformations, especially on the way to extended polyaromatic components of carbon-rich materials.

Associate content

Supporting Information

Full experimental details, 1H NMR, 13C NMR, NMR spectra for all of the prepared compounds, X-ray crystallographlic data for selected products, and computational details for all calculated structures.

Acknowledgments: The financial support of the National Science Foundation is gratefully acknowledged by M. A. P. (CHE-2003411, UAlbany) and I. A. (CHE-2102579, FSU). This project used resources provided by the Materials Characterization Laboratory (FSU075000MAC) at the FSU Department of Chemistry and Biochemistry. R.G.P. expresses her deep appreciation for the financial and scientific support of Prof. Dr. Peter Chen. D.T.E. and R.G.P. gratefully acknowledge the financial support of the ETH Zurich and the ETH Zurich Foundation, and thank Dr. Eno Paenurk for his assistance with the BC-Wizard program. D.T.E is a 2019 ESOP scholar; R.G.P. is a Branco Weiss Fellow and a Horev Fellow.

References

(1) Wu, J.; Pisula, W.; Müllen, K. Graphenes as Potential Material for Electronics. *Chem. Rev.* **2007**, *107* (3), 718–747. https://doi.org/10.1021/cr068010r.

(2) Zhi, L.; Müllen, K. A Bottom-up Approach from Molecular Nanographenes to Unconventional Carbon Materials. *J. Mater. Chem.* **2008**, *18* (13), 1472. https://doi.org/10.1039/b717585j.

(3) Narita, A.; Feng, X.; Hernandez, Y.; Jensen, S. A.; Bonn, M.; Yang, H.; Verzhbitskiy, I. A.; Casiraghi, C.; Hansen, M. R.; Koch, A. H. R.; Fytas, G.; Ivasenko, O.; Li, B.; Mali, K. S.; Balandina, T.; Mahesh, S.; De Feyter, S.; Müllen, K. Synthesis of Structurally Well-Defined and Liquid-Phase-Processable Graphene Nanoribbons. *Nature Chem* **2014**, *6* (2), 126–132. https://doi.org/10.1038/nchem.1819.

(4) Steiner, A.-K.; Amsharov, K. Y. The Rolling-Up of Oligophenylenes to Nanographenes by a HF-Zipping Approach. *Angew. Chem. Int. Ed.* **2017**, *56* (46), 14732–14736. https://doi.org/10.1002/anie.201707272.

(5) Senese, A.; Chalifoux, W. Nanographene and Graphene Nanoribbon Synthesis via Alkyne Benzannulations. *Molecules* **2018**, *24* (1), 118. https://doi.org/10.3390/molecules24010118.

(6) von Kugelgen, S.; Piskun, I.; Griffin, J. H.; Eckdahl, C. T.; Jarenwattananon, N. N.; Fischer, F. R. Templated Synthesis of End-Functionalized Graphene Nanoribbons through Living Ring-Opening Alkyne Metathesis Polymerization. *J. Am. Chem. Soc.* **2019**, *141* (28), 11050–11058. https://doi.org/10.1021/jacs.9b01805.

(7) Rizzo, D. J.; Veber, G.; Cao, T.; Bronner, C.; Chen, T.; Zhao, F.; Rodriguez, H.; Louie, S. G.; Crommie, M. F.; Fischer, F. R. Topological Band Engineering of Graphene Nanoribbons. *Nature* **2018**, *560* (7717), 204–208. https://doi.org/10.1038/s41586-018-0376-8.

(8) Liu, J.; Li, B.-W.; Tan, Y.-Z.; Giannakopoulos, A.; Sanchez-Sanchez, C.; Beljonne, D.; Ruffieux, P.; Fasel, R.; Feng, X.; Müllen, K. Toward Cove-Edged Low Band Gap Graphene Nanoribbons. *J. Am. Chem. Soc.* **2015**, *137* (18), 6097–6103. https://doi.org/10.1021/jacs.5b03017.

(9) Yang, X.; Dou, X.; Rouhanipour, A.; Zhi, L.; Räder, H. J.; Müllen, K. Two-Dimensional Graphene Nanoribbons. *J. Am. Chem. Soc.* **2008**, *130* (13), 4216–4217. https://doi.org/10.1021/ja710234t.

(10) Bronner, C.; Marangoni, T.; Rizzo, D. J.; Durr, R. A.; Jørgensen, J. H.; Fischer, F. R.; Crommie, M. F. Iodine versus Bromine Functionalization for Bottom-Up Graphene Nanoribbon Growth: Role of Diffusion. *J. Phys. Chem. C* **2017**, *121* (34), 18490–18495. https://doi.org/10.1021/acs.jpcc.7b02896.

(11) Liu, Z.; Chen, Z.; Wang, C.; Wang, H. I.; Wuttke, M.; Wang, X.-Y.; Bonn, M.; Chi, L.; Narita, A.; Müllen, K. Bottom-Up, On-Surface-Synthesized Armchair Graphene Nanoribbons for Ultra-High-Power Micro-Supercapacitors. *J. Am. Chem. Soc.* **2020**, *142* (42), 17881–17886. https://doi.org/10.1021/jacs.0c06109.

(12) Luong, D. X.; Bets, K. V.; Algozeeb, W. A.; Stanford, M. G.; Kittrell, C.; Chen, W.; Salvatierra, R. V.; Ren, M.; McHugh, E. A.; Advincula, P. A.; Wang, Z.; Bhatt, M.; Guo, H.; Mancevski, V.; Shahsavari, R.; Yakobson, B. I.; Tour, J. M. Gram-Scale Bottom-up Flash Graphene Synthesis. *Nature* **2020**, *577* (7792), 647–651. https://doi.org/10.1038/s41586-020-1938-0.

(13) Matsuoka, W.; Ito, H.; Sarlah, D.; Itami, K. Diversity-Oriented Synthesis of Nanographenes Enabled by Dearomative Annulative π-Extension. *Nat Commun* **2021**, *12* (1), 3940. https://doi.org/10.1038/s41467-021-24261-y.

(14) Dressler, J. J.; Zhou, Z.; Marshall, J. L.; Kishi, R.; Takamuku, S.; Wei, Z.; Spisak, S. N.; Nakano, M.; Petrukhina, M. A.; Haley, M. M. Synthesis of the Unknown Indeno[1,2- *a*]Fluorene Regioisomer: Crystallographic Characterization of Its Dianion. *Angew. Chem. Int. Ed.* **2017**, *56* (48), 15363–15367. https://doi.org/10.1002/anie.201709282.

(15) Zhang, Y.; Zhu, Y.; Lan, D.; Pun, S. H.; Zhou, Z.; Wei, Z.; Wang, Y.; Lee, H. K.; Lin, C.; Wang, J.; Petrukhina, M. A.; Li, Q.; Miao, Q. Charging a Negatively Curved Nanographene and Its Covalent Network. *J. Am. Chem. Soc.* **2021**, *143* (13), 5231–5238. https://doi.org/10.1021/jacs.1c01642.

(16) Zhou, Z.; Zhu, Y.; Wei, Z.; Bergner, J.; Neiß, C.; Doloczki, S.; Görling, A.; Kivala, M.; Petrukhina, M. A. Reduction of Π-Expanded Cyclooctatetraene with Lithium: Stabilization of the Tetra-Anion through Internal Li $^{+}$ Coordination. *Angew. Chem. Int. Ed.* **2021**, *60* (7), 3510–3514. https://doi.org/10.1002/anie.202013353.

(17) Zhou, Z.; Fernández-García, J. M.; Zhu, Y.; Evans, P. J.; Rodríguez, R.; Crassous, J.; Wei, Z.; Fernández, I.; Petrukhina, M. A.; Martín, N. Site-Specific Reduction-Induced Hydrogenation of a Helical Bilayer Nanographene with K and Rb Metals: Electron Multiaddition and Selective Rb $^{+}$ Complexation. *Angew Chem Int Ed* **2022**, *61* (10). https://doi.org/10.1002/anie.202115747.

(18) Lawton, R. G.; Barth, W. E. Synthesis of Corannulene. *J. Am. Chem. Soc.* **1971**, *93* (7), 1730–1745. https://doi.org/10.1021/ja00736a028.

(19) Hanson, J. C.; Nordman, C. E. The Crystal and Molecular Structure of Corannulene, C20H10. *Acta Crystallogr B Struct Crystallogr Cryst Chem* **1976**, *32* (4), 1147–1153. https://doi.org/10.1107/S0567740876012430.

(20) Kroto, H. W.; Heath, J. R.; O'Brien, S. C.; Curl, R. F.; Smalley, R. E. C60: Buckminsterfullerene. *Nature* **1985**, *318* (6042), 162–163. https://doi.org/10.1038/318162a0.

(21) Petrukhina, M. A.; Andreini, K. W.; Mack, J.; Scott, L. T. X-Ray Quality Geometries of Geodesic Polyarenes from Theoretical Calculations: What Levels of Theory Are Reliable? *J. Org. Chem.* **2005**, *70* (14), 5713–5716. https://doi.org/10.1021/jo050233e.

(22) Wu, Y.-T.; Siegel, J. S. Aromatic Molecular-Bowl Hydrocarbons: Synthetic Derivatives, Their Structures, and Physical Properties. *Chem. Rev.* **2006**, *106* (12), 4843–4867. https://doi.org/10.1021/cr050554q.

(23) Tsefrikas, V. M.; Scott, L. T. Geodesic Polyarenes by Flash Vacuum Pyrolysis. *Chem. Rev.* **2006**, *106* (12), 4868–4884. https://doi.org/10.1021/cr050553y.

(24) Amaya, T.; Hirao, T. A Molecular Bowl Sumanene. *Chem. Commun.* **2011**, *47* (38), 10524. https://doi.org/10.1039/c1cc12532j.

(25) Sygula, A. Chemistry on a Half-Shell: Synthesis and Derivatization of Buckybowls. *Eur. J. Org. Chem.* **2011**, *2011* (9), 1611–1625. https://doi.org/10.1002/ejoc.201001585.

(26) Scott, L. T.; Jackson, E. A.; Zhang, Q.; Steinberg, B. D.; Bancu, M.; Li, B. A Short, Rigid, Structurally Pure Carbon Nanotube by Stepwise Chemical Synthesis. *J. Am. Chem. Soc.* **2012**, *134* (1), 107–110. https://doi.org/10.1021/ja209461g.

(27) Wu, T.-C.; Hsin, H.-J.; Kuo, M.-Y.; Li, C.-H.; Wu, Y.-T. Synthesis and Structural Analysis of a Highly Curved Buckybowl Containing Corannulene and Sumanene Fragments. *J. Am. Chem. Soc.* **2011**, *133* (41), 16319–16321. https://doi.org/10.1021/ja2067725.

(28) Higashibayashi, S.; Sakurai, H. Synthesis of Sumanene and Related Buckybowls. *Chem. Lett.* **2011**, *40* (2), 122–128. https://doi.org/10.1246/cl.2011.122.

(29) Zabula, A. V.; Spisak, S. N.; Filatov, A. S.; Rogachev, A. Yu.; Petrukhina, M. A. Record Alkali Metal Intercalation by Highly Charged Corannulene. *Acc. Chem. Res.* **2018**, *51* (6), 1541–1549. https://doi.org/10.1021/acs.accounts.8b00141.

(30) Lu, R.; Wu, S.; Yang, L.; Gao, W.; Qu, H.; Wang, X.; Chen, J.; Tang, C.; Shi, H.; Cao, X. Stable Diindeno-Fused Corannulene Regioisomers with Open-Shell Singlet Ground States and Large Diradical Characters. *Angew. Chem. Int. Ed.* **2019**, *58* (23), 7600–7605. https://doi.org/10.1002/anie.201902028.

(31) Zou, Y.; Zeng, W.; Gopalakrishna, T. Y.; Han, Y.; Jiang, Q.; Wu, J. Dicyclopenta[4,3,2,1- *Ghi* :4′,3′,2′,1′- *Pqr*]Perylene: A Bowl-Shaped Fragment of Fullerene C_{70} with Global Antiaromaticity. *J. Am. Chem. Soc.* **2019**, *141* (18), 7266–7270. https://doi.org/10.1021/jacs.9b03169.

(32) Tanaka, Y.; Fukui, N.; Shinokubo, H. As-Indaceno[3,2,1,8,7,6-Ghijklm]Terrylene as a near-Infrared Absorbing C70-Fragment. *Nat Commun* **2020**, *11* (1), 3873. https://doi.org/10.1038/s41467-020-17684-6.

(33) Li, Q.; Hamamoto, Y.; Kwek, G.; Xing, B.; Li, Y.; Ito, S. Diazapentabenzocorannulenium: A Hydrophilic/Biophilic Cationic Buckybowl. *Angewandte Chemie Intl Edit* **2022**, *61* (4). https://doi.org/10.1002/anie.202112638.

(34) Miyoshi, H.; Sugiura, R.; Kishi, R.; Spisak, S. N.; Wei, Z.; Muranaka, A.; Uchiyama, M.; Kobayashi, N.; Chatterjee, S.; Ie, Y.; Hisaki, I.; Petrukhina, M. A.; Nishinaga, T.; Nakano, M.; Tobe, Y. Dianion and Dication of Tetracyclopentatetraphenylene as Decoupled Annulene-within-an-Annulene Models. *Angew Chem Int Ed* **2022**, *61* (6). https://doi.org/10.1002/anie.202115316.

(35) Zhou, Z.; Kawade, R. K.; Wei, Z.; Kuriakose, F.; Üngör, Ö.; Jo, M.; Shatruk, M.; Gershoni-Poranne, R.; Petrukhina, M. A.; Alabugin, I. V. Negative Charge as a Lens for Concentrating Antiaromaticity: Using a Pentagonal "Defect" and Helicene Strain for Cyclizations. *Angewandte Chemie International Edition* **2020**, *59* (3), 1256–1262. https://doi.org/10.1002/anie.201911319.

(36) Pati, K.; dos Passos Gomes, G.; Harris, T.; Hughes, A.; Phan, H.; Banerjee, T.; Hanson, K.; Alabugin, I. V. Traceless Directing Groups in Radical Cascades: From Oligoalkynes to Fused Helicenes without Tethered Initiators. *J. Am. Chem. Soc.* **2015**, *137* (3), 1165–1180. https://doi.org/10.1021/ja510563d.

(37) King, B. T.; Kroulík, J.; Robertson, C. R.; Rempala, P.; Hilton, C. L.; Korinek, J. D.; Gortari, L. M. Controlling the Scholl Reaction. *J. Org. Chem.* **2007**, *72* (7), 2279–2288. https://doi.org/10.1021/jo061515x.

(38) Rempala, P.; Kroulík, J.; King, B. T. A Slippery Slope: Mechanistic Analysis of the Intramolecular Scholl Reaction of Hexaphenylbenzene. *J. Am. Chem. Soc.* **2004**, *126* (46), 15002–15003. https://doi.org/10.1021/ja046513d.

(39) Rempala, P.; Kroulík, J.; King, B. T. Investigation of the Mechanism of the Intramolecular Scholl Reaction of Contiguous Phenylbenzenes. *J. Org. Chem.* **2006**, *71* (14), 5067–5081. https://doi.org/10.1021/jo0526744.

(40) Ajaz, A.; McLaughlin, E. C.; Skraba, S. L.; Thamatam, R.; Johnson, R. P. Phenyl Shifts in Substituted Arenes via *Ipso* Arenium Ions. *J. Org. Chem.* **2012**, *77* (21), 9487–9495. https://doi.org/10.1021/jo301848g.

(41) Zhai, L.; Shukla, R.; Wadumethrige, S. H.; Rathore, R. Probing the Arenium-Ion (ProtonTransfer) versus the Cation-Radical (Electron Transfer) Mechanism of Scholl Reaction Using DDQ as Oxidant. *J. Org. Chem.* **2010**, *75* (14), 4748–4760. https://doi.org/10.1021/jo100611k.

(42) Little, M. S.; Yeates, S. G.; Alwattar, A. A.; Heard, K. W. J.; Raftery, J.; Edwards, A. C.; Parry, Adam. V. S.; Quayle, P. Insights into the Scholl Coupling Reaction: A Key Transformation of Relevance to the Synthesis of Graphenes and Related Systems: Insights into the Scholl Coupling Reaction: A Key Transformation of Relevance to the Synthesis of Graphenes and Related Systems. *Eur. J. Org. Chem.* **2017**, *2017* (13), 1694–1703. https://doi.org/10.1002/ejoc.201601580.

(43) Segawa, Y.; Maekawa, T.; Itami, K. Synthesis of Extended Π-Systems through C–H Activation. *Angew. Chem. Int. Ed.* **2015**, *54* (1), 66–81. https://doi.org/10.1002/anie.201403729.

(44) Sánchez-Sánchez, C.; Martínez, J. I.; Ruiz del Arbol, N.; Ruffieux, P.; Fasel, R.; López, M. F.; de Andres, P. L.; Martín-Gago, J. Á. On-Surface Hydrogen-Induced Covalent Coupling of Polycyclic Aromatic Hydrocarbons via a Superhydrogenated Intermediate. *J. Am. Chem. Soc.* **2019**, *141* (8), 3550–3557. https://doi.org/10.1021/jacs.8b12239.

(45) Sánchez-Sánchez, C.; Dienel, T.; Deniz, O.; Ruffieux, P.; Berger, R.; Feng, X.; Müllen, K.; Fasel, R. Purely Armchair or Partially Chiral: Noncontact Atomic Force Microscopy Characterization of Dibromo-Bianthryl-Based Graphene Nanoribbons Grown on Cu(111). *ACS Nano* **2016**, *10* (8), 8006–8011. https://doi.org/10.1021/acsnano.6b04025.

(46) Treier, M.; Pignedoli, C. A.; Laino, T.; Rieger, R.; Müllen, K.; Passerone, D.; Fasel, R. Surface-Assisted Cyclodehydrogenation Provides a Synthetic Route towards Easily Processable and Chemically Tailored Nanographenes. *Nature Chem* **2011**, *3* (1), 61–67. https://doi.org/10.1038/nchem.891.

(47) Pavliček, N.; Mistry, A.; Majzik, Z.; Moll, N.; Meyer, G.; Fox, D. J.; Gross, L. Synthesis and Characterization of Triangulene. *Nature Nanotech* **2017**, *12* (4), 308–311. https://doi.org/10.1038/nnano.2016.305.

(48) Urbano, A. Recent Developments in the Synthesis of Helicene-Like Molecules. *Angew. Chem. Int. Ed.* **2003**, *42* (34), 3986–3989. https://doi.org/10.1002/anie.200301667.

(49) Shen, Y.; Chen, C.-F. Helicenes: Synthesis and Applications. *Chem. Rev.* **2012**, *112* (3), 1463–1535. https://doi.org/10.1021/cr200087r.

(50) Gingras, M. One Hundred Years of Helicene Chemistry. Part 1: Non-Stereoselective Syntheses of Carbohelicenes. *Chem. Soc. Rev.* **2013**, *42* (3), 968–1006. https://doi.org/10.1039/C2CS35154D.

(51) Gingras, M.; Félix, G.; Peresutti, R. One Hundred Years of Helicene Chemistry. Part 2: Stereoselective Syntheses and Chiral Separations of Carbohelicenes. *Chem. Soc. Rev.* **2013**, *42* (3), 1007–1050. https://doi.org/10.1039/C2CS35111K.

(52) Gingras, M. One Hundred Years of Helicene Chemistry. Part 3: Applications and Properties of Carbohelicenes. *Chem. Soc. Rev.* **2013**, *42* (3), 1051–1095. https://doi.org/10.1039/C2CS35134J.

(53) Rickhaus, M.; Mayor, M.; Juríček, M. Strain-Induced Helical Chirality in Polyaromatic Systems. *Chem. Soc. Rev.* **2016**, *45* (6), 1542–1556. https://doi.org/10.1039/C5CS00620A.

(54) Dhbaibi, K.; Favereau, L.; Crassous, J. Enantioenriched Helicenes and Helicenoids Containing Main-Group Elements (B, Si, N, P). *Chem. Rev.* **2019**, *119* (14), 8846–8953. https://doi.org/10.1021/acs.chemrev.9b00033.

(55) Mori, T. Chiroptical Properties of Symmetric Double, Triple, and Multiple Helicenes. *Chem. Rev.* **2021**, *121* (4), 2373–2412. https://doi.org/10.1021/acs.chemrev.0c01017.

(56) Gilbert, A. M.; Katz, T. J.; Geiger, W. E.; Robben, M. P.; Rheingold, A. L. Synthesis and Properties of an Optically Active Helical Bis-Cobaltocenium Ion. *J. Am. Chem. Soc.* **1993**, *115* (8), 3199–3211. https://doi.org/10.1021/ja00061a019.

(57) Nuckolls, C.; Katz, T. J.; Verbiest, T.; Elshocht, S. V.; Kuball, H.-G.; Kiesewalter, S.; Lovinger, A. J.; Persoons, A. Circular Dichroism and UV−Visible Absorption Spectra of the Langmuir−Blodgett Films of an Aggregating Helicene. *J. Am. Chem. Soc.* **1998**, *120* (34), 8656–8660. https://doi.org/10.1021/ja981757h.

(58) Hassey, R.; Swain, E. J.; Hammer, N. I.; Venkataraman, D.; Barnes, M. D. Probing the Chiroptical Response of a Single Molecule. *Science* **2006**, *314* (5804), 1437–1439. https://doi.org/10.1126/science.1134231.

(59) Anger, E.; Srebro, M.; Vanthuyne, N.; Toupet, L.; Rigaut, S.; Roussel, C.; Autschbach, J.; Crassous, J.; Réau, R. Ruthenium-Vinylhelicenes: Remote Metal-Based Enhancement and Redox Switching of the Chiroptical Properties of a Helicene Core. *J. Am. Chem. Soc.* **2012**, *134* (38), 15628–15631. https://doi.org/10.1021/ja304424t.

(60) Yang, Y.; da Costa, R. C.; Smilgies, D.; Campbell, A. J.; Fuchter, M. J. Induction of Circularly Polarized Electroluminescence from an Achiral Light-Emitting Polymer via a Chiral Small-Molecule Dopant. *Adv. Mater.* **2013**, *25* (18), 2624–2628. https://doi.org/10.1002/adma.201204961.

(61) Yang, Y.; da Costa, R. C.; Fuchter, M. J.; Campbell, A. J. Circularly Polarized Light Detection by a Chiral Organic Semiconductor Transistor. *Nature Photon* **2013**, *7* (8), 634–638. https://doi.org/10.1038/nphoton.2013.176.

(62) Zhang, X.; Clennan, E. L.; Arulsamy, N. Photophysical and Electrochemical Characterization of a Helical Viologen, *N* , *N* ′-Dimethyl-5,10-Diaza[5]Helicene. *Org. Lett.* **2014**, *16* (17), 4610–4613. https://doi.org/10.1021/ol502180y.

(63) Zhong, Y.; Kumar, B.; Oh, S.; Trinh, M. T.; Wu, Y.; Elbert, K.; Li, P.; Zhu, X.; Xiao, S.; Ng, F.; Steigerwald, M. L.; Nuckolls, C. Helical Ribbons for Molecular Electronics. *J. Am. Chem. Soc.* **2014**, *136* (22), 8122–8130. https://doi.org/10.1021/ja503533y.

(64) Li, C.; Cho, J.; Yamada, K.; Hashizume, D.; Araoka, F.; Takezoe, H.; Aida, T.; Ishida, Y. Macroscopic Ordering of Helical Pores for Arraying Guest Molecules Noncentrosymmetrically. *Nat Commun* **2015**, *6* (1), 8418. https://doi.org/10.1038/ncomms9418.

(65) Storch, J.; Zadny, J.; Strasak, T.; Kubala, M.; Sykora, J.; Dusek, M.; Cirkva, V.; Matejka, P.; Krbal, M.; Vacek, J. Synthesis and Characterization of a Helicene-Based Imidazolium Salt and Its Application in Organic Molecular Electronics. *Chem. Eur. J.* **2015**, *21* (6), 2343–2347. https://doi.org/10.1002/chem.201405239.

(66) Ravat, P.; Šolomek, T.; Rickhaus, M.; Häussinger, D.; Neuburger, M.; Baumgarten, M.; Juríček, M. Cethrene: A Helically Chiral Biradicaloid Isomer of Heptazethrene. *Angew. Chem. Int. Ed.* **2016**, *55* (3), 1183–1186. https://doi.org/10.1002/anie.201507961.

(67) Vacek, J.; Hrbáč, J.; Strašák, T.; Církva, V.; Sýkora, J.; Fekete, L.; Pokorný, J.; Bulíř, J.; Hromadová, M.; Crassous, J.; Storch, J. Anodic Deposition of Enantiopure Hexahelicene Layers. *ChemElectroChem* **2018**, *5* (15), 2080–2088. https://doi.org/10.1002/celc.201800565.

(68) Karras, M.; Holec, J.; Bednárová, L.; Pohl, R.; Schmidt, B.; Stará, I. G.; Starý, I. Asymmetric Synthesis of Nonracemic 2-Amino[6]Helicenes and Their Self-Assembly into Langmuir Films. *J. Org. Chem.* **2018**, *83* (10), 5523–5538. https://doi.org/10.1021/acs.joc.8b00538.

(69) Anetai, H.; Takeda, T.; Hoshino, N.; Kobayashi, H.; Saito, N.; Shigeno, M.; Yamaguchi, M.; Akutagawa, T. Ferroelectric Alkylamide-Substituted Helicene Derivative with Two-Dimensional Hydrogen-Bonding Lamellar Phase. *J. Am. Chem. Soc.* **2019**, *141* (6), 2391–2397. https://doi.org/10.1021/jacs.8b11222.

(70) Kalachyova, Y.; Guselnikova, O.; Elashnikov, R.; Panov, I.; Žádný, J.; Církva, V.; Storch, J.; Sykora, J.; Zaruba, K.; Švorčík, V.; Lyutakov, O. Helicene-SPP-Based Chiral Plasmonic Hybrid Structure: Toward Direct Enantiomers SERS Discrimination. *ACS Appl. Mater. Interfaces* **2019**, *11* (1), 1555–1562. https://doi.org/10.1021/acsami.8b15520.

(71) Církva, V.; Jakubík, P.; Strašák, T.; Hrbáč, J.; Sýkora, J.; Císařová, I.; Vacek, J.; Žádný, J.; Storch, J. Preparation and Physicochemical Properties of [6]Helicenes Fluorinated at Terminal Rings. *J. Org. Chem.* **2019**, *84* (4), 1980–1993. https://doi.org/10.1021/acs.joc.8b02870.

(72) Nakakuki, Y.; Hirose, T.; Matsuda, K. Logical Design of Small HOMO–LUMO Gap: Tetrabenzo[*f* , *Jk* , *Mn* , *r*][7]Helicene as a Small-Molecule Near-Infrared Emitter. *Org. Lett.* **2022**, *24* (2), 648–652. https://doi.org/10.1021/acs.orglett.1c04095.

(73) Chalifoux, W. A.; Sitaula, P.; Malone, R. J.; Longhi, G.; Abbate, S.; Gualtieri, E.; Lucotti, A.; Tommasini, M.; Franzini, R.; Villani, C.; Catalano, V. J. Π-Extended Helical Nanographenes: Synthesis and Photophysical Properties of Naphtho[1,2- *a*]Pyrenes**. *European J Organic Chem* **2022**. https://doi.org/10.1002/ejoc.202101466.

(74) Fujikawa, T.; Segawa, Y.; Itami, K. Synthesis and Structural Features of Quadruple Helicenes: Highly Distorted π Systems Enabled by Accumulation of Helical Repulsions. *J. Am. Chem. Soc.* **2016**, *138* (10), 3587–3595. https://doi.org/10.1021/jacs.6b01303.

(75) Qiu, Z.; Asako, S.; Hu, Y.; Ju, C.-W.; Liu, T.; Rondin, L.; Schollmeyer, D.; Lauret, J.-S.; Müllen, K.; Narita, A. Negatively Curved Nanographene with Heptagonal and [5]Helicene Units. *J. Am. Chem. Soc.* **2020**, *142* (35), 14814–14819. https://doi.org/10.1021/jacs.0c05504.

(76) Wei, L.; Deng, X.; Yu, X.; Li, X.; Wang, W.; Zhang, C.; Xiao, J. Double π-Extended Helicene Derivatives Containing Pentagonal Rings: Synthesis, Crystal Analyses, and Photophysics. *J. Org. Chem.* **2021**, *86* (24), 17535–17542. https://doi.org/10.1021/acs.joc.1c00989.

(77) Medel, M. A.; Tapia, R.; Blanco, V.; Miguel, D.; Morcillo, S. P.; Campaña, A. G. Octagon-Embedded Carbohelicene as a Chiral Motif for Circularly Polarized Luminescence Emission of Saddle-Helix Nanographenes. *Angew. Chem. Int. Ed.* **2021**, *60* (11), 6094–6100. https://doi.org/10.1002/anie.202015368.

(78) Swain, A. K.; Radacki, K.; Braunschweig, H.; Ravat, P. Pyrene-Fused [7]Helicenes Connected Via Hexagonal and Heptagonal Rings: Stereospecific Synthesis and Chiroptical Properties. *J. Org. Chem.* **2022**, *87* (2), 993–1000. https://doi.org/10.1021/acs.joc.1c02281.

(79) Duan, C.; Zhang, J.; Xiang, J.; Yang, X.; Gao, X. Azulene-Embedded [*n*]Helicenes (*n* =5, 6 and 7). *Angew Chem Int Ed* **2022**. https://doi.org/10.1002/anie.202201494.

(80) Field, J. E.; Muller, G.; Riehl, J. P.; Venkataraman, D. Circularly Polarized Luminescence from Bridged Triarylamine Helicenes. *J. Am. Chem. Soc.* **2003**, *125* (39), 11808–11809. https://doi.org/10.1021/ja035626e.

(81) Collins, S. K.; Vachon, M. P. Unlocking the Potential of Thiaheterohelicenes: Chemical Synthesis as the Key. *Org. Biomol. Chem.* **2006**, *4* (13), 2518. https://doi.org/10.1039/b603305a.

(82) Míšek, J.; Teplý, F.; Stará, I. G.; Tichý, M.; Šaman, D.; Císařová, I.; Vojtíšek, P.; Starý, I. A Straightforward Route to Helically Chiral N-Heteroaromatic Compounds: Practical Synthesis of Racemic 1,14-Diaza[5]Helicene and Optically Pure 1- and 2-Aza[6]Helicenes. *Angew. Chem. Int. Ed.* **2008**, *47* (17), 3188–3191. https://doi.org/10.1002/anie.200705463.

(83) Žádný, J.; Jančařík, A.; Andronova, A.; Šámal, M.; Vacek Chocholoušová, J.; Vacek, J.; Pohl, R.; Šaman, D.; Císařová, I.; Stará, I. G.; Starý, I. A General Approach to Optically Pure [5]-, [6]-, and [7]Heterohelicenes. *Angew. Chem. Int. Ed.* **2012**, *51* (24), 5857–5861. https://doi.org/10.1002/anie.201108307.

(84) Waghray, D.; de Vet, C.; Karypidou, K.; Dehaen, W. Oxidative Transformation to Naphthodithiophene and Thia[7]Helicenes by Intramolecular Scholl Reaction of Substituted 1,2-Bis(2-Thienyl)Benzene Precursors. *J. Org. Chem.* **2013**, *78* (22), 11147–11154. https://doi.org/10.1021/jo401807x.

(85) Nakamura, K.; Furumi, S.; Takeuchi, M.; Shibuya, T.; Tanaka, K. Enantioselective Synthesis and Enhanced Circularly Polarized Luminescence of S-Shaped Double Azahelicenes. *J. Am. Chem. Soc.* **2014**, *136* (15), 5555–5558. https://doi.org/10.1021/ja500841f.

(86) Wang, X.-Y.; Wang, X.-C.; Narita, A.; Wagner, M.; Cao, X.-Y.; Feng, X.; Müllen, K. Synthesis, Structure, and Chiroptical Properties of a Double [7]Heterohelicene. *J. Am. Chem. Soc.* **2016**, *138* (39), 12783–12786. https://doi.org/10.1021/jacs.6b08664.

(87) Evoniuk, C. J.; Gomes, G. dos P.; Hill, S. P.; Fujita, S.; Hanson, K.; Alabugin, I. V. Coupling N–H Deprotonation, C–H Activation, and Oxidation: Metal-Free C(Sp ^{3})–H Aminations with Unprotected Anilines. *J. Am. Chem. Soc.* **2017**, *139* (45), 16210–16221. https://doi.org/10.1021/jacs.7b07519.

(88) Nejedlý, J.; Šámal, M.; Rybáček, J.; Tobrmanová, M.; Szydlo, F.; Coudret, C.; Neumeier, M.; Vacek, J.; Vacek Chocholoušová, J.; Buděšínský, M.; Šaman, D.; Bednárová, L.; Sieger, L.; Stará, I. G.; Starý, I. Synthesis of Long Oxahelicenes by Polycyclization in a Flow Reactor. *Angew. Chem. Int. Ed.* **2017**, *56* (21), 5839–5843. https://doi.org/10.1002/anie.201700341.

(89) Li, J.-K.; Chen, X.-Y.; Guo, Y.-L.; Wang, X.-C.; Sue, A. C.-H.; Cao, X.-Y.; Wang, X.-Y. B,N-Embedded Double Hetero[7]Helicenes with Strong Chiroptical Responses in the Visible Light Region. *J. Am. Chem. Soc.* **2021**, *143* (43), 17958–17963. https://doi.org/10.1021/jacs.1c09058.

(90) Zhou, Z.; Wang, X.; Wei, Z.; Müllen, K.; Petrukhina, M. A. Charging OBO-Fused Double [5]Helicene with Electrons. *Angew. Chem. Int. Ed.* **2019**, *58* (42), 14969–14973. https://doi.org/10.1002/anie.201908658.

(91) Lousen, B.; Pedersen, S. K.; Bols, P.; Hansen, K. H.; Pedersen, M. R.; Hammerich, O.; Bondarchuk, S.; Minaev, B.; Baryshnikov, G. V.; Ågren, H.; Pittelkow, M. Compressing a Non-Planar Aromatic Heterocyclic [7]Helicene to a Planar Hetero[8]Circulene. *Chem. Eur. J.* **2020**, *26* (22), 4935–4940. https://doi.org/10.1002/chem.201905339.

(92) Chernick, E. T.; Tykwinski, R. R. Carbon-Rich Nanostructures: The Conversion of Acetylenes into Materials: THE CONVERSION OF ACETYLENES INTO MATERIALS. *J. Phys. Org. Chem.* **2013**, *26* (9), 742–749. https://doi.org/10.1002/poc.3160.

(93) Jančařík, A.; Rybáček, J.; Cocq, K.; Vacek Chocholoušová, J.; Vacek, J.; Pohl, R.; Bednárová, L.; Fiedler, P.; Císařová, I.; Stará, I. G.; Starý, I. Rapid Access to Dibenzohelicenes and Their Functionalized Derivatives. *Angew. Chem. Int. Ed.* **2013**, *52* (38), 9970–9975. https://doi.org/10.1002/anie.201301739.

(94) Mohamed, R. K.; Mondal, S.; Guerrera, J. V.; Eaton, T. M.; Albrecht-Schmitt, T. E.; Shatruk, M.; Alabugin, I. V. Alkynes as Linchpins for the Additive Annulation of Biphenyls: Convergent Construction of Functionalized Fused Helicenes. *Angew. Chem. Int. Ed.* **2016**, *55* (39), 12054–12058. https://doi.org/10.1002/anie.201606330.

(95) Pati, K.; dos Passos Gomes, G.; Alabugin, I. V. Combining Traceless Directing Groups with Hybridization Control of Radical Reactivity: From Skipped Enynes to Defect-Free Hexagonal Frameworks. *Angew. Chem. Int. Ed.* **2016**, *55* (38), 11633–11637. https://doi.org/10.1002/anie.201605799.

(96) Klívar, J.; Jančařík, A.; Šaman, D.; Pohl, R.; Fiedler, P.; Bednárová, L.; Starý, I.; Stará, I. G. [2+2+2] Cycloisomerisation of Aromatic Cyanodiynes in the Synthesis of Pyridohelicenes and Their Analogues. *Chem. Eur. J.* **2016**, *22* (40), 14401–14405. https://doi.org/10.1002/chem.201602747.

(97) Šámal, M.; Chercheja, S.; Rybáček, J.; Vacek Chocholoušová, J.; Vacek, J.; Bednárová, L.; Šaman, D.; Stará, I. G.; Starý, I. An Ultimate Stereocontrol in Asymmetric Synthesis of Optically Pure Fully Aromatic Helicenes. *J. Am. Chem. Soc.* **2015**, *137* (26), 8469–8474. https://doi.org/10.1021/jacs.5b02794.

(98) Sánchez, I. G.; Šámal, M.; Nejedlý, J.; Karras, M.; Klívar, J.; Rybáček, J.; Buděšínský, M.; Bednárová, L.; Seidlerová, B.; Stará, I. G.; Starý, I. Oxahelicene NHC Ligands in the Asymmetric Synthesis of Nonracemic Helicenes. *Chem. Commun.* **2017**, *53* (31), 4370–4373. https://doi.org/10.1039/C7CC00781G.

(99) Alabugin, I. V.; Gonzalez-Rodriguez, E. Alkyne Origami: Folding Oligoalkynes into Polyaromatics. *Acc. Chem. Res.* **2018**, *51* (5), 1206–1219. https://doi.org/10.1021/acs.accounts.8b00026.

(100) Stará, I. G.; Starý, I. Helically Chiral Aromatics: The Synthesis of Helicenes by [2 + 2 + 2] Cycloisomerization of π-Electron Systems. *Acc. Chem. Res.* **2020**, *53* (1), 144–158. https://doi.org/10.1021/acs.accounts.9b00364.

(101) Palata, O.; Andronova, A.; Šámal, M.; Nejedlý, J.; Rybáček, J.; Buděšínský, M.; Bednárová, L.; Pospíšil, L.; Císařová, I.; Starý, I.; Stará, I. G. Synthesis of (Di)Thiahelicenes and Dithiophenohelicenes by [2+2+2] Cycloisomerization of Alkynes. *Helvetica Chimica Acta* **2022**. https://doi.org/10.1002/hlca.202100225.

(102) Zhou, Z.; Wei, Z.; Tokimaru, Y.; Ito, S.; Nozaki, K.; Petrukhina, M. A. Stepwise Reduction of Azapentabenzocorannulene. *Angew. Chem. Int. Ed.* **2019**, *58* (35), 12107–12111. https://doi.org/10.1002/anie.201906748.

(103) Zabula, A. V.; Spisak, S. N.; Filatov, A. S.; Rogachev, A. Yu.; Clérac, R.; Petrukhina, M. A. Supramolecular Trap for a Transient Corannulene Trianion. *Chem. Sci.* **2016**, *7* (3), 1954–1961. https://doi.org/10.1039/C5SC04385A.

(104) Zhou, Z.; Wei, Z.; Schaub, T. A.; Jasti, R.; Petrukhina, M. A. Structural Deformation and Host–Guest Properties of Doubly-Reduced Cycloparaphenylenes, [*n*]CPPs $^{2-}$ (*n* = 6, 8, 10, and 12). *Chem. Sci.* **2020**, *11* (35), 9395–9401. https://doi.org/10.1039/D0SC03072D.

(105) Zhou, Z.; Wei, Z.; Ikemoto, K.; Sato, S.; Isobe, H.; Petrukhina, M. A. Chemical Reduction of a Nanosized [6]Cyclo-2,7-naphthylene Macrocycle. *Angew. Chem. Int. Ed.* **2021**, *60* (20), 11201–11205. https://doi.org/10.1002/anie.202100942.

(106) Zhou, Z.; Üngör, Ö.; Wei, Z.; Shatruk, M.; Tsybizova, A.; Gershoni-Poranne, R.; Petrukhina, M. A. Tuning Magnetic Interactions Between Triphenylene Radicals by Variation of Crystal Packing in Structures with Alkali Metal Counterions. *Inorg. Chem.* **2021**, *60* (19), 14844–14853. https://doi.org/10.1021/acs.inorgchem.1c02139.

(107) Schleyer, P. v R.; Maerker, C.; Dransfeld, A.; Jiao, H.; van Eikema Hommes, N. J. R. Nucleus-Independent Chemical Shifts: A Simple and Efficient Aromaticity Probe. *J. Am. Chem. Soc.* **1996**, *118* (26), 6317–6318. https://doi.org/10.1021/JA960582D.

(108) Gershoni-Poranne, R.; Stanger, A. Magnetic Criteria of Aromaticity. *Chem. Soc. Rev.* **2015**, *44* (18), 6597–6615.

(109) Gershoni-Poranne, R.; Stanger, A. 4 - NICS—Nucleus-Independent Chemical Shift. In *Aromaticity: Modern Computational Methods and Applications*; Fernandez, I., Ed.; Elsevier, 2021; pp 99–154. https://doi.org/10.1016/B978-0-12-822723-7.00004-2.

(110) Paenurk, E.; Gershoni-Poranne, R. Simple and Efficient Visualization of Aromaticity: Bond Currents Calculated from NICS Values. *Phys. Chem. Chem. Phys.* **2022**. https://doi.org/10.1039/D1CP05757J.

(111) Aprahamian, I.; Bodwell, G. J.; Fleming, J. J.; Manning, G. P.; Mannion, M. R.; Sheradsky, T.; Vermeij, R. J.; Rabinovitz, M. "The Great Escape" from Antiaromaticity: Reduction of Strained Pyrenes. *J. Am. Chem. Soc.* **2003**, *125* (7), 1720–1721. https://doi.org/10.1021/ja0291991.

(112) Peterson, P. W.; Shevchenko, N.; Breiner, B.; Manoharan, M.; Lufti, F.; Delaune, J.; Kingsley, M.; Kovnir, K.; Alabugin, I. V. Orbital Crossings Activated through Electron Injection: Opening Communication between Orthogonal Orbitals in Anionic C1–C5 Cyclizations of Enediynes. *J. Am. Chem. Soc.* **2016**, *138* (48), 15617–15628. https://doi.org/10.1021/jacs.6b08540.

(113) Papadakis, R.; Ottosson, H. The Excited State Antiaromatic Benzene Ring: A Molecular Mr Hyde? *Chem. Soc. Rev.* **2015**, *44* (18), 6472–6493. https://doi.org/10.1039/C5CS00057B.

(114) Mohamed, R. K.; Mondal, S.; Jorner, K.; Delgado, T. F.; Lobodin, V. V.; Ottosson, H.; Alabugin, I. V. The Missing C $_1$ –C $_5$ Cycloaromatization Reaction: Triplet State Antiaromaticity Relief and Self-Terminating Photorelease of Formaldehyde for Synthesis of Fulvenes from Enynes. *J. Am. Chem. Soc.* **2015**, *137* (49), 15441–15450. https://doi.org/10.1021/jacs.5b07448.

(115) Slanina, T.; Ayub, R.; Toldo, J.; Sundell, J.; Rabten, W.; Nicaso, M.; Alabugin, I.; Fdez. Galván, I.; Gupta, A. K.; Lindh, R.; Orthaber, A.; Lewis, R. J.; Grönberg, G.; Bergman, J.; Ottosson, H. Impact of Excited-State Antiaromaticity Relief in a Fundamental Benzene Photoreaction Leading to Substituted Bicyclo[3.1.0]Hexenes. *J. Am. Chem. Soc.* **2020**, *142* (25), 10942–10954. https://doi.org/10.1021/jacs.9b13769.

(116) Karas, L. J.; Campbell, A. T.; Alabugin, I. V.; Wu, J. I. Antiaromaticity Gain Activates Tropone and Nonbenzenoid Aromatics as Normal-Electron-Demand Diels–Alder Dienes. *Org. Lett.* **2020**, *22* (18), 7083–7087. https://doi.org/10.1021/acs.orglett.0c02343.

(117) Frisch, M. J.; Trucks, G. W.; Schlegel, H. B.; Scuseria, G. E.; Robb, M. A.; Cheeseman, J. R.; Scalmani, G.; Barone, V.; Mennucci, B.; Petersson, G. A.; et al. Gaussian 09, Revision D.01. *Gaussian, Inc., Wallingford CT* **2016**.

(118) Lee, C.; Yang, W.; Parr, R. G. Development of the Colle-Salvetti Correlation-Energy Formula into a Functional of the Electron Density. *Physical Review B* **1988**, *37* (2), 785–789. https://doi.org/10.1103/PhysRevB.37.785.

(119) Becke, A. D. Density-functional Thermochemistry. III. The Role of Exact Exchange. *The Journal of Chemical Physics* **1993**, *98* (7), 5648–5652. https://doi.org/10.1063/1.464913.

(120) Binkley, J. S.; Pople, J. A.; Hehre, W. J. Self-Consistent Molecular Orbital Methods. 21. Small Split-Valence Basis Sets for First-Row Elements. *J. Am. Chem. Soc.* **1980**, *102* (3), 939–947. https://doi.org/10.1021/ja00523a008.

(121) Frisch, M. J.; Pople, J. A.; Binkley, J. S. Self-consistent Molecular Orbital Methods 25. Supplementary Functions for Gaussian Basis Sets. *J. Chem. Phys.* **1984**, *80* (7), 3265–3269. https://doi.org/10.1063/1.447079.

(122) Grimme, S.; Antony, J.; Ehrlich, S.; Krieg, H. A Consistent and Accurate Ab Initio Parametrization of Density Functional Dispersion Correction (DFT-D) for the 94 Elements H-Pu. *J. Chem. Phys.* **2010**, *132* (15), 154104. https://doi.org/10.1063/1.3382344.

(123) Smith, D. G. A.; Burns, L. A.; Patkowski, K.; Sherrill, C. D. Revised Damping Parameters for the D3 Dispersion Correction to Density Functional Theory. *J. Phys. Chem. Lett.* **2016**, *7* (12), 2197–2203. https://doi.org/10.1021/acs.jpclett.6b00780.

(124) Gershoni-Poranne, R.; Stanger, A. The NICS-XY-Scan: Identification of Local and Global Ring Currents in Multi- Ring Systems. *Chem. - Eur. J.* **2014**, *20* (19), 5673–5688. https://doi.org/10.1002/chem.201304307.

(125) Rahalkar, A. P.; Stanger, A. "Aroma", Http://Schulich.Technion.Ac.Il/Amnon_Stanger.Htm.

(126) Stanger, A. Nucleus-Independent Chemical Shifts (NICS): Distance Dependence and Revised Criteria for Aromaticity and Antiaromaticity. *Journal of Organic Chemistry* **2006**, *71* (3), 883–893. https://doi.org/10.1021/jo051746o.

(127) Stanger, A. Obtaining Relative Induced Ring Currents Quantitatively from NICS. *Journal of Organic Chemistry* **2010**, *75* (7), 2281–2288. https://doi.org/10.1021/jo1000753.

(128) Chen, Z.; Wannere, C. S.; Corminboeuf, C.; Puchta, R.; Schleyer, P. von R. Nucleus-Independent Chemical Shifts (NICS) as an Aromaticity Criterion. *Chem. Rev.* **2005**, *105* (10), 3842–3888. https://doi.org/10.1021/cr030088+.

(129) Ditchfield, R. Self-Consistent Perturbation Theory of Diamagnetism. *Molecular Physics* **1974**, *27* (4), 789–807. https://doi.org/10.1080/00268977400100711.

(130) Schreckenbach, G.; Ziegler, T. Calculation of NMR Shielding Tensors Using Gauge-Including Atomic Orbitals and Modern Density Functional Theory. *J. Phys. Chem.* **1995**, *99* (2), 606–611. https://doi.org/10.1021/j100002a024.

(131) Paenurk, E.; Gershoni-Poranne, R. *BC-WIzard*; https://gitlab.com/porannegroup/bcwizard/-/releases, 2022.

(132) *The PyMOL Molecular Graphics System*; Schrödinger, LLC., 2014.

TOC Graphic